INL/EXT-14-33562
Revision 0

The Development of an INL Capability for High Temperature Flow, Heat Transfer, and Thermal Energy Storage with Applications in Advanced Small Modular Reactors, High Temperature Heat Exchangers, Hybrid Energy Systems, and Dynamic Grid Energy Storage Concepts

Xiaodong Sun, Xiaoqin Zhang, Inhun Kim
(The Ohio State University)

James O'Brien, Piyush Sabharwall
(Idaho National Laboratory)

October 2014

The INL is a U.S. Department of Energy National Laboratory
operated by Battelle Energy Alliance

INL/EXT-14-33562

The Development of an INL Capability for High Temperature Flow, Heat Transfer, and Thermal Energy Storage with Applications in Advanced Small Modular Reactors, High Temperature Heat Exchangers, Hybrid Energy Systems, and Dynamic Grid Energy Storage Concepts

Xiaodong Sun, Xiaoqin Zhang, Inhun Kim
(The Ohio State University)

James O'Brien, Piyush Sabharwall
(Idaho National Laboratory)

October 2014

Idaho National Laboratory
Idaho Falls, Idaho 83415

http://www.inl.gov

Prepared for the
U.S. Department of Energy
Under DOE Idaho Operations Office
Contract DE-AC07-05ID14517

SUMMARY

The overall goal of this project is to support Idaho National Laboratory in developing a new advanced high-temperature multi-fluid multi-loop test facility that is aimed at investigating fluid flow and heat transfer, material corrosion, heat exchanger characteristics and instrumentation performance, among others, for nuclear applications. Specifically, preliminary research has been performed at The Ohio State University in the following areas:

1. A review of fluoride molten salts' characteristics in thermal, corrosive, and compatibility performances. A recommendation for a salt selection is provided. Material candidates for both molten salt and helium flow loop have been identified.
2. A conceptual facility design that satisfies the multi-loop (two-coolant loops [i.e., fluoride molten salts and helium]) multi-purpose (two operation modes [i.e., forced and natural circulation]) requirements. Schematic models are presented. The thermal hydraulic performances in a preliminary PCHE design have been estimated.
3. An introduction of computational methods and models for pipe heat loss analysis and cases studies. Recommendations on insulation material selection have been provided.
4. An analysis of pipe pressure rating and sizing. Preliminary recommendations on pipe size selection have been provided.
5. A review of molten fluoride salt preparation and chemistry control. An introduction to the experience from the Molten Salt Reactor Experiment at Oak Ridge National Laboratory has been provided.
6. A review of some instruments and components to be used in the facility. Flowmeters and Grayloc connectors have been included.

This report primarily presents the conclusions drawn from the extensive review of literatures in material selections and the facility design progress at the current stage. It provides some useful guidelines in insulation material and pipe size selection, as well as an introductory review of facility process and components.

CONTENTS

FIGURES

TABLES

ACRONYMS

ANP	Aircraft Nuclear Propulsion
ANSI	American National Standards Institute
API	American Petroleum Institute
ASME	American Society of Mechanical Engineers
ASTM	American Society for Testing Materials
BWT	Bundle Waveguide Technology System
CUI	Corrosion Under Insulation
DRACS	Direct Reactor Auxiliary Cooling System
FHR	Fluoride salt-cooled High-temperature Reactor
FOM	Figure of Merit
HE	Helium Flow Loop
HF	Hydrogen Flouride
HTDF	High-Temperature DRACS test Facility
HTHF	High-Temperature Helium test Facility
HTTS	Heat Transfer Test Section
HX	Heat Exchanger
IHX	Intermediate Heat Exchanger
IIG	Industrial Insulation Group, LLC
INL	Idaho National Laboratory
LMTD	Logarithmic Mean Temperature Difference
MS	Molten Salt
MSRE	Molten Salt Reactor Experiment
MT	Microtherm Moulded Products
MW	Min Wool
NIST	National Institute of Standards and Technology
NPS	Nominal Pipe Size
OD	Outmost Diameter
OSU	The Ohio State University
ORNL	Oak Ridge National Laboratory
PCHE	Printed Circuit Heat Exchanger
Ra	Rayleigh number
SCH	Schedule
SS	Stainless Steel
UW-Madison	University of Wisconsin-Madison

The Development of an INL Capability for High Temperature Flow, Heat Transfer, and Thermal Energy Storage with Applications in Advanced Small Modular Reactors, High Temperature Heat Exchangers, Hybrid Energy Systems, and Dynamic Grid Energy Storage Concepts

1. INTRODUCTION

This project is aiming at supporting Idaho National Laboratory (INL) in developing a new advanced high-temperature multi-fluid multi-loop test facility to investigate heat transfer, material corrosion, and heat exchanger (HX) characteristics, among others for nuclear applications. The project at The Ohio State University (OSU) started officially on January 16, 2014. At the current stage, an investigation in molten salts selection, structural material selection, conceptual facility design, scaling analysis, heat loss rate analysis and insulation material selection, pressure rating and pipe sizing, fluoride salt chemistry control, and instruments and components have been performed. This report primarily centers on six parts:

1. The review of the material issues concerning molten fluoride salts characteristics in thermal performance, corrosion, and compatibility with structural materials. The molten salt characteristics are identified through a comparison of salts' thermal properties and potential cost to narrow down the candidates. The structural material candidates are identified with corrosion issues discussed.
2. The conceptual design of the facility used for both forced and natural circulation configurations. A conceptual design of the two-loop facility is provided, along with estimated thermal-hydraulic performance of some components. A scaling analysis for the forced circulation mode of the designed facility is presented.
3. The heat loss analysis and thermal insulation materials selection. A physical model and computational methodology is provided for MATLAB programming. An introduction to insulation materials is presented. Several cases of heat loss analysis have been carried out.
4. The review of pipe pressure ratings and the recommendation of pipe sizing. Different pipe dimensions have been studied in terms of pressure ratings and economic sizing, and a preliminary recommendation on pipe size is given.
5. The chemistry control of molten fluoride salt. The experience from the Oak Ridge National Laboratory (ORNL) has been summarized. A new gas treatment using NF_3 instead of hydrogen fluoride (HF)/H_2 combination has been introduced.
6. The introduction of several components and instruments. Flow meters used for helium and molten salt loop, as well as grayloc connectors have been introduced.

2. MOLTEN SALT SELECTION

2.1 Molten Salt Characteristics

A molten salt selection study is essential to the multi-purpose molten salt flow loop facility. Generally, for the application to the Fluoride salt-cooled High-temperature Reactors (FHRs) secondary loop coolant, several fluoride and chloride molten salts are typically considered with regard to their thermal and hydraulic properties. In this project, eight salt candidates have been taken into account, and their properties are summarized in Table 1 according to Williams et al. [1].

Table 1. Summary of the properties of the eight candidate coolants.

Coolant	Formula Weight (g/mol)	Melting Point (C)	1173 K Vapor Pressure (kPa)	Heat Transfer Properties at 973 K				
				$\rho \times 10^{-3}$ Density (kg/m^3)	c_p Heat Capacity (kJ/kg-K)	ρc_p (MJ/m^3-K)	μ Viscosity (g/m-s)	k Thermal Conductivity (W/m-K)
LiF-NaF-KF	41.3	454	0.093	2.02	1.88	3.80	2.9	0.92
LiF-NaF-ZrF_4	84.2	436	~0.7	2.92	1.46	4.26	6.9	0.53
NaF-ZrF_4	92.7	500	0.666	3.14	1.17	3.67	5.1	0.49
KF-ZrF_4	103.9	390	0.160	2.80	1.05	2.94	<5.1	0.45
NaF-$NaBF_4$	104.4	385	1270	1.75	1.50	2.63	0.90	0.40
LiCl-KCl	55.5	355	0.773	1.52	1.20	1.82	1.15	0.42
NaCl-$MgCl_2$	73.7	445	<0.33	1.68	1.09	1.83	1.36	0.50
KCl-$MgCl_2$	81.4	426	<0.27	1.66	1.15	1.91	1.40	0.40

In general, practical considerations for the molten salt application to FHRs may include the thermochemical properties (melting point, vapor pressure, density, and heat capacity) and transport properties (viscosity and thermal conductivity) of the salts. The melting point below 773 K and low vapor pressure is preferred. From the experience of ORNL research, it is desirable to achieve low vapor pressure below 0.2 kPa for the equipment designs and cover-gas system. In addition, higher density, higher heating capacity, higher thermal conductivity, and lower viscosity [2] are preferred in choosing a molten salt coolant for the facility design. The heat transport capability is measured by the volumetric heat capacity ρc_p as shown below:

$$\dot{Q} = \dot{m} c_p \Delta T = (\rho u A) c_p \Delta T = (\rho c_p)(u A \Delta T) \tag{1}$$

where $\dot{Q}$ is the heat transfer rate in coolant; $\dot{m}$ is the coolant mass flow rate; u and A are the mean coolant velocity and flow area; ΔT is the temperature rise. Higher density assures higher capability in transporting heat per volume, but it may impose extra demands on pumping equipment if the salt is too dense. Higher heating capacity greatly decreases the required mass flow rate and improves heat transport performance. Higher thermal conductivity provides better heat transfer performance. Low viscosity leads to less friction loss, thus the pumping power demand will decrease.

It seems that the thermal and hydraulic requirements on the properties do not pose severe limitations on the selection of the salts. However, the combination of the properties may have great influence on the entire loop heat transfer and transport performance. To evaluate the important thermal performance of different salts, six requirements have been developed in the report by Sabharwall et al. [2] (Figure 1).

These six requirements are evaluated by six figures of merit (FOMs) that assign the superior candidate with a lower numerical value except that a higher value for FOM_{th} is preferred, which are listed as follows:

Heat transfer performance FOM_{th}: $FOM_{ht} = k^{0.6} \rho^{0.58} c_p^{\ 0.4} \mu^{-0.47}$

Pumping power FOM_p: $FOM_p = \rho^{-2} c_p^{\ -0.28} \mu^{0.2}$

Coolant volume FOM_{cv}: $FOM_{cv} = \rho^{-0.48} c_p^{\ -1.16} \mu^{0.1}$

Material volume FOM_{ccv}: $FOM_{ccv} = p \cdot \rho^{-0.84} c_p^{\ -1.16} \mu^{0.1}$

Heat loss FOM_{hl}: $FOM_{hl} = k^{0.6}\rho^{0.34}c_p{}^{0.06}\mu^{-0.44}$

Temperature drop FOM_{dt}: $FOM_{dt} = k^{0.6}\rho^{0.34}c_p{}^{0.06}\mu^{-0.44}$

where p is internal pressure.

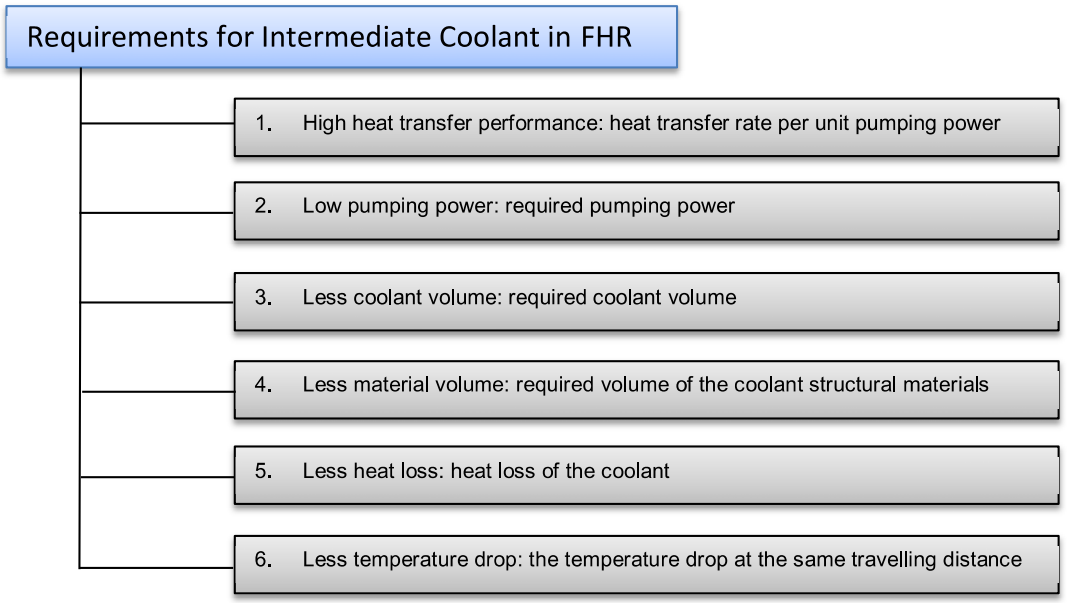

Figure 1. General thermal-hydraulic requirements for the intermediate coolant selection [2].

In addition to these six FOMs, other typical FOMs for natural and forced convections are examined to further justify the salt selection in heat transfer comparison. A lower value of the following FOMs indicates preferred properties. These FOMs are defined by Bonilla [1] as:

Turbulent forced convection FOM_{ft}: $FOM_{ft} = \rho^{-2}c_p{}^{-2.8}\mu^{0.2}$

Turbulent free convection FOM_{nt}: $FOM_{nt} = \beta^{-2}\rho^{-0.72}c_p{}^{-0.648}\mu^{0.2}$

Laminar free convection FOM_{nf}: $FOM_{nl} = \beta^{-0.5}\rho^{-1}c_p{}^{0.5}\mu$

where $\beta = 1/\rho \cdot d\rho/dT$ is the thermal expansion coefficient.

Table 2 shows a comparison of the thermal-hydraulic characteristics of four molten salts based on the FOMs to the reference of water at 25°C and 0.1 MPa for the first six and the water at 300°C for the last three. All of the FOMs were estimated based on a temperature 700°C of the salt. In brief, FLiNaK can be one of the most promising salt candidates. According to the comparison, FLiNaK displays preferred characteristics in general, but shows the worst performance in heat loss and temperature drop, which could be compensated by appropriate means, such as additional insulation layers. NaF-ZrF_4 also can be a good selection with regard to thermal-hydraulic performance if the melting temperature is not a high priority in consideration. KF-ZrF_4 is perhaps a compromised option because it is inferior to FLiNaK and NaF-ZrF_4, but exhibits relatively better characteristics compared with the rest of the salts. In fact, this salt is selected as the secondary loop salt in a Direct Reactor Auxiliary Cooling System (DRACS) High-Temperature test Facility (HTDF) at OSU. In addition, from the FOMs' comparison it is noted that NaF-$NaBF_4$ indicates some good characteristics as well, but has not been considered as one of the molten salt coolant options due to its extremely high vapor pressure, which is not desired in the facility design. In

the literature, KCl-MgCl is usually mentioned as one of the molten salts of interest. Nevertheless, few substantially preferred characteristics have been observed in the comparison. To date, the selections have been limited to four salt types: FLiNaK, NaF-ZrF_4, KF-ZrF_4, and KCl-MgCl.

Table 2. Comparison of FOMs for the molten salt candidates [1][2].

Coolant	FOM_{th}	FOM_p	FOM_{cv}	FOM_{ccv}	FOM_{hl}	FOM_{dt}	FOM_{ft}	FOM_{nt}	FOM_{nl}
LiF-NaF-KF	0.80	2.87	1.57	1.57	0.92	0.92	1.13	13.3	6.61
LiF-NaF-ZrF_4	0.40	5.36	2.05	2.05	0.50	0.50	1.42	13.9	9.01
NaF-ZrF_4	0.45	5.02	1.98	1.98	0.56	0.56	1.98	14.7	7.90
KF-ZrF_4	0.38	8.69	2.49	2.49	0.51	0.51	3.39	16.7	9.05
NaF-$NaBF_4$	0.71	5.66	2.04	2.04	0.88	0.88	2.20	14.7	4.31
LiCl-KCl	0.55	14.99	3.07	3.07	0.76	0.76	5.88	20.8	7.15
NaCl-$MgCl_2$	0.58	16.26	3.18	3.18	0.81	0.81	6.40	21.7	7.81
KCl-$MgCl_2$	0.50	14.30	3.02	3.02	0.70	0.70	5.66	21.1	7.74

2.2 Cost Comparison

The cost of the molten salts is one of the most important factors for selection of an appropriate salt for the facility. In general, the cost of the salts for the high-temperature salt systems is comprised of the acquisition cost of the raw materials for the salt coolant and the associated processing cost, etc. It would be challenging to precisely determine the total cost for the facility design before the construction because of the varying market price and the unknown total volume of the salts. However, as far as the price of the raw salt material is concerned, estimation is available to help guide the selection. Williams et al. has listed a summary of some salt constituent prices based on the survey conducted by ORNL [1][3]. Table 3 shows such a price estimation of the salts. A more recent price summary is included as Table 4 and Table 5.

Table 3. ORNL 1971 price estimation of salt coolants (partial).

Coolant	Composition (%)	Melting Point (C)	Cost (US$/kg)	Cost (US$/liter)
NaF-KF-ZrF4		385	4.6	11.7
Mole percent	10-48-42			
Weight percent	4-27-69			
^{7}LiF-NaF-KF		454	11.3	24.1
Mole percent	46-11.5-42.5			
Weight percent	29-12-59			

Table 4. Commodity prices for selected materials.

Material	Commodity Price (US$/kg)	Price of Contained Metal (US$/kg metal)	Source
LiF	17.00	63.5	USGS 1995 Minerals Yearbook
NaF	1.37	2.56	Chemical Marketing Reporter, Vol.267, No.12 (2005)
KF	4.54	6.74	Chemical Marketing Reporter, Vol.267, No.12 (2005)
KCl	0.125	0.24	Chemical Marketing Reporter, Vol.267, No.12 (2005)
$MgCl_2$	0.36	1.41	Chemical Marketing Reporter, Vol.267, No.12 (2005)
Zr metal	30.80	30.80	USGS 2000 Minerals Yearbook

Table 5. Estimated raw material costs for various salt mixtures based on prices in Table 3.

Salt Mixture	Composition (mol %)	Composition (wt %)	Raw Material Cost (US$/kg salt mixture)	Cost per Volume (US$/liter at 973 K)
LiF-NaF-KF	46.5-11.5-42	29-12-59	7.82	15.79
NaF-ZrF4	59.5-40.5	27-73	4.02	12.63
KF-ZrF4	58-42	32.5-67.5	4.85	13.58
KCl-$MgCl_2$	68-32	62-38	0.21	0.35

Based on the values provided from Williams [1], we can conclude that (1) KCl-$MgCl_2$ is the least expensive salt among the eight; (2) all of the salt mixtures with Zr or LiF become expensive due to their high price of the metal; (3) despite a higher price of FLiNaK in terms of per kilogram, the price per liter is similar to the salt mixtures containing Zr. The last conclusion indicates that Zr-containing molten salts are not greatly competitive with FLiNaK in terms of the acquisition cost per volume because the total content of salt mixtures in the facility depends on the total volume other than the total mass.

This is further justified by Sabharwall et al. [2]. In that report the relative total coolant cost in terms of the coolant volume factor for various salts has been summarized as shown in Table 6. It is evident that Zr-containing salts do not have an advantage in price any longer. According to the comparison, KCl-$MgCl_2$ shows the most attractive price, which is about two orders of magnitude less than that of the remaining candidates. The prices also indicate that a more comprehensive investigation is needed to select the economical salts in terms of the total cost, including pumping power requirement, containment material cost, etc.

A survey of the cost of three fluoride salts has been conducted at OSU recently (in 2013). Quotes provided by vendors have been compared, and the lowest prices of these salts in terms of per kilogram as well as the corresponding cost per volume of the salts are listed in Table 7. It shows that the salts containing ZrF_4 greatly increase the potential cost. In addition, the price of FLiNaK is the lowest.

Table 6. Raw material costs for the candidate salt mixtures and relative total cost estimation.

Coolant	Cost/volume ($/liter)	Cost/volume ($/$m^3$)	FOM_{cv}	Relative Coolant Total Cost ($/$m^3$)
LiF-NaF-KF	15.79	15,790	1.57	24,724
NaF-ZrF4	12.63	12,630	1.98	25,053
KF-ZrF4	13.58	13,580	2.49	33,862
KCl-$MgCl_2$	0.35	350	3.02	1,335

Table 7. Quote from a cost survey at OSU and corresponding cost per unit volume for three salt candidates.

	LiF	NaF	KF	ZrF_4
Quote ($/kg)	56	100	30	495
	FLiNaK	NaF- ZrF_4	KF- ZrF_4	
Cost per Volume ($/$m^3$)	~92	~1219	~963	

2.3 Conclusion and Recommendation

From the analysis above, it is clear that there are many factors to be considered in determining the final selection of the salts to be used in the facility. Although some FOMs are offered to estimate the salts' characteristics in thermal-physical properties and performances in the loop, they do not manage to

address the comprehensive judgment for ultimate salt selection, with respect to economic considerations and compatibility issues. However, it is safely concluded that FLiNaK is currently considered as the relatively suitable molten salt choice according to the thermal features analysis and price comparison as well as the experience and data available from previous research. Therefore, FLiNaK is recommended at this stage as the salt coolant for the INL's multi-loop test facility and used as a reference salt in the following analysis and design.

3. STRUCTURAL MATERIAL SELECTION

3.1 Structural Material Candidates

Based on the experience with the High-Temperature Helium test Facility (HTHF) and the construction of High-Temperature DRACS test Facility at OSU, six structural material candidates have been identified: Alloy 617, Alloy 600, Alloy 800H, Alloy 230, Hastelloy N/INOR-8, and Stainless Steel (SS) 316 [14][15][16]. These materials have superior features in high-temperature strength, corrosion resistance to oxidation and commercial readiness in manufacturing. Some candidates have already been of widespread use in industries even for the applications in nuclear reactor systems. In this section, characteristics and applications of these alloy candidates are investigated briefly. The alloys' compositions are summarized in Table 8.

3.1.1 Alloy 617

Alloy 617 is a solid-solution, strengthened, nickel-chromium-cobalt molybdenum alloy with an exceptional combination of high-temperature strength and oxidation resistance. It also has excellent corrosion resistance and is readily fabricated and welded. The most attractive feature of Alloy 617 is the combination of high strength and high-oxidation resistance at temperatures over 980°C/1800°F. It is widely used as component material of ducting, combustion cans in aircraft, and land-based gas turbines. It is also used in chemical industry, and fossil-fueled and nuclear power-generating plants.

Alloy 617 possesses high mechanical properties over a broad range of temperatures. Especially at elevated temperature, it has outstanding characteristics in the high levels of creep-rupture strength combined with the resistance to the high-temperature corrosions. Hence, Alloy 617 is suitable for long-term operation and high-stress environment.

Table 8. Composition of structural material candidates.

	Quantity in Alloy, w/o					
Components	**617**	**600**	**800H**	**230**	**H N**	**SS 316**
Nickel	44.5 min.	72.0 min.	30.0-35.0	57 as balance	71	10.0-14.0
Chromium	20.0-24.0	14.0-17.0	19.0-23.0	22	7	16.0-18.0
Iron	3.0 max.	6.0-10.0	39.5 min.	3 max.	5 max.	as balance
Molybdenum	8.0-10.0			2	16	2.0-3.0
Manganese	1.0 max.	1.0 max.		0.5	0.80 max.	2.00 max.
Carbon	0.05-0.15	0.15 max.	0.05-0.10	0.1	0.08 max.	0.08 max.
Silicon	1.0 max.	0.5 max.		0.4	1 max.	0.75 max.
Sulfur	0.015 max.					0.03 max.
Copper	0.5 max.	0.5 max.			0.35 max.	
Cobalt	10.0-15.0			5 max.	0.20 max.	
Aluminum	0.8-1.5		0.15-0.60	0.3	Al+Ti = 0.35 max.	

Components	Quantity in Alloy, w/o					
	617	600	800H	230	H N	SS 316
Titanium	0.6 max		0.15-0.60			
Boron	0.006 max			0.015 max		
Tungsten				14	0.50 max	
Others				La = 0.02		P = 0.045 max N = 0.10 max

3.1.2 Alloy 600

Alloy 600 is a nickel-chromium-iron alloy with excellent mechanical properties and desirable combination of high strength and good processability. It is a standard engineering material for the applications where resistance to corrosion and high temperature is required. Due to that excellent characteristic, it is commonly used in chemical industries with various corrosive environments as well as in heat-treating industries with applications to retorts, muffles, roller hearths, and other furnace components. In the aeronautical field, Alloy 600 is used for a variety of engines and airframe components for high-temperature operation. It is also used for construction of light-water reactors to withstand corrosions in water system.

The composition of Alloy 600 assures the resistance to a variety of corrosives. The chromium content provides resistance to oxidizing conditions while nickel content provides considerable resistance under reducing conditions. The protective oxide coating formed at the alloy's surface can significantly withstand cyclic exposure to the extremely high temperature (up to 980°C/1800°F) with negligible weight loss.

3.1.3 Alloy 800H

Alloy 800H is a nickel-iron-chromium alloy with relative low nickel content. It is introduced to the market as a heat- and corrosion-resistant alloy with application to furnace components and equipment, petrochemical furnace cracker tubes and sheathing for electrical heating elements, high-temperature heat exchangers in gas-cooled nuclear reactors, etc. In brief, the exceptional mechanical properties of alloy 800H, combined with the resistance to high-temperature corrosion, are useful for applications to long-term operations at elevated temperature and corrosive environments.

Alloy 800H is characterized by its high creep and rupture strengths, which is competitive with Alloy 617. It also exhibits attractive features in corrosion resistance. It displays good performance when exposed to high-temperature reactions such as oxidation and carburization. The chromium-nickel-promoted formation of the protective surface oxide is capable of withstanding cyclic high-temperature exposure, especially at very high temperature regions, which is competitive with Alloy 600.

3.1.4 Haynes Alloy 230

Alloy 230 is a solid-solution, strengthened, nickel-chromium-tungsten-molybdenum alloy that is characterized by its high-temperature strength, resistance to oxidizing environments exposure up to 1149°C (2100°F) and long-term thermal stability. It is readily formed and is castable as well. The application of Alloy 230 includes a wide range of component applications in aerospace and power industry. It is used for combustion cans, transition ducts, thermocouple sheaths, and gas turbine components. It is also used in chemical industries and industrial heating industries for various kinds of components, for instance, high-temperature heat exchangers, ducts, recuperator internals, and many more.

Alloy 230 is probably one of the excellent alloys in terms of high-temperature strength capability. It shows particularly effective superiority in long-term applications at temperatures of 649°C (1200°F),

outlasting stainless steels and nickel alloys. Alloy 230 also displays good resistance to both air and combustion gas oxidizing environments for long-term exposure at temperature up to 1149°C (2100°F). In other types of corrosions such as aqueous corrosion, it is competitive among some of the alloys mentioned above.

3.1.5 Hastelloy N/ INOR-8 (H N)

Hastelloy N is a nickel-based alloy that was invented at ORNL as a container material for molten fluoride salts. It has been proved to be one of the most promising vessel materials for the fluoride salts application. There were a large number of corrosion test data available at ORNL, and the results showed that the corrosion attack was negligible even at very high temperature under long-term exposure. Alloy N is capable of being supplied in several common forms including sheet, plate and bar.

3.1.6 Stainless Steel 316 (SS 316)

Type 316 stainless steel is widely used in many applications requiring corrosion resistance to Type 304, or good elevated temperature strength. Typically, SS 316 is used for applications of exhaust manifolds, furnace parts, heat exchangers, valve and pump trim, chemical equipment, pharmaceutical and photographic equipment, parts exposed to marine atmospheres and tubing, etc. SS 316 exhibits improved chloride corrosion resistance and other good chemical resistance to most agents used in the paper, petroleum, food, and dairy industry. Exposed to acetic, formic, phosphoric and tartaric acids along with some concentrations of bromide and iodide solutions, SS 316 can display good corrosion resistance.

3.2 Molten Salt Loop Piping Material Selection

For the application to the heat transfer medium in the secondary loop other than the one in the reactor core, the molten salt requires structural materials effectively resistant to corrosion by the fluoride salt. It is confirmed from previous studies that alloys containing considerable quantities of chromium can be attacked by fluoride salts, mainly because of the removal of chromium in the alloy towards fluoride salts, which is basically caused by the impurities or oxides present in the salts [4][5]. Other corrosion mechanisms include the activity gradient and temperature gradient-driven corrosions. These corrosion behaviors are critical to the structural material selection in the molten salt loops.

The corrosion driven by the oxidizing contaminants in the molten salts, usually moisture or impurities, will dominate the corrosion process in the initial stage. It is clear that when the impurities or oxidants are exhausted, this type of corrosion may cease. H_2O is one of the most deleterious contaminants in fluoride salts from the standpoint of this type of corrosion. The reaction of alkali fluorides with moisture follows the ones below [6]:

$$\begin{aligned} MF(l) + H_2O(g) &\rightarrow MOH(l) + HF(g) \\ 2MF(l) + H_2O(g) &\rightarrow M_2O(l) + 2HF(g) \end{aligned} \tag{2}$$

Typically due to the oxidation of chromium with the impurities, which is also known as “chromium depletion,” the concentration of chromium at the surface adherent protective layer may decrease, leading to the chromium diffusion from subsurface of the alloys and the formation of voids at subsurface area. The depth of the void formation strongly depends on the operating temperatures and the composition of the salts. This mechanism may cause rapid corrosion attack to the alloy at the very beginning, but eventually it decreases as the corrosion rate is linearly dependent on time. This can be explained by the fact that the chromium-depletion corrosion will cease when all oxidants are expended and then mass transfer between the structure surface and salts is predominant, which is only characterized by the linear time dependence. In the static corrosion tests [6] the corrosion phenomena driven by chromium removal have been substantiated.

This mass transfer is concerned with intrinsic tendency of galvanic corrosion due to the differing electromotive potentials and differential solubility due to the thermal gradients. The difference in the free

energy of the salt constituents and the alloy fluorides is the key driving force for corrosion [2]. It is believed that alloys whose constituents have less negative free energies of fluoride formation are less prone to corrosion [2]. With respect to the temperature gradient driven corrosion, it was observed that crystal precipitation of chromium occurred at the cold leg in the ORNL early tests. Theoretically, there was a relationship between chromium concentration equilibrium in the salts and the temperature. The chromium concentration at the hot leg was very high, in the case of FLiNaK, whereas at cold leg, it experienced smaller concentration, leading to the precipitation of crystal metal that could induce corrosion. Such a test was done in the fuel salts, but it was believed that this indirect observation could be applied to coolant salts since the low uranium content was present [3].

An extensive investigation in the selection of the construction material for molten-salt reactors has been conducted in ORNL [3]. In the literature, there are several material candidates proposed in the compatibility studies, which are SS 316, Inconel particularly 600, and INOR-8/Hastelloy N respectively. The corrosion testing results for various kinds of salts are available in the ORNL MSRE program reports, from which the testing results for FLiNaK have been summarized in Table 9. Furthermore, the static tests of materials with FLiNaK [6] in University of Wisconsin-Madison (UW-Madison) has given a guide in the selection of material based on different criteria, which is summarized in Table 10.

Table 9. Summary of corrosion testing results for salts (FLiNaK) without uranium.

Loop No.	Alloy	Salt	Duration (h)	T_{max}/°C	Corrosion Depth (mil)	ORNL Report No.
116	316SS	FLiNaK	500	815	4	1294
348	Inconel	FLiNaK	500	815	7	1816
1214	Inconel	FLiNaK	4673	677	13	2684
9344-2	Inconel	FLiNaK	8760	649	8	2890
9344-2	Inconel	FLiNaK	8735	649	8	3215
1175	Inconel	FLiNaK	1000	607	1	2474
1208	INOR-8	FLiNaK	8760	677	1	2799
1165	INOR-8	FLiNaK	1340	677	0	2551
1194	INOR-8	FLiNaK	1000	607	0	2551

Table 10. The ranking of material selection with FLiNaK suggested by Olson et al. [5].

Criteria	Rankings (Better Performance to Worse)					
Sample mass loss	230	617	800H	HX	HN	Ni-210
Dissolved chromium content	800H	230	HX	HN	Ni-210	
Grain boundary attack	230	800H	HX	617	HN	Ni-210

In conclusion, it is still challenging to choose an appropriate structural material since corrosion test data from the circulation loops for alloys are limited except Inconel 600 and Hastelloy N, and the recommendations by the corrosion tests performed by UW-Madison are merely based on static studies. It is recognized that the factors other than intrinsic mechanism and chromium content driven corrosion are likely to play an important role in corrosion issues. However, with the information provided in the preceding section and selection requirement mentioned above, Haynes 230, Inconel 600, and H-N are recommended as reasonable candidates for the molten salt loop construction material. According to the composition information, they contain relative low chromium content, which can mitigate the initial rapid corrosion with impurities. The available test results demonstrate their preferred corrosion resistance. Additionally, their widespread applications assure their capability in high-temperature mechanical

properties. Nevertheless there is still uncertainty as to whether these alloys can withstand extremely high temperature and correspondingly severe corrosion in dynamic operations. More investigation is called for to address these issues.

3.3 Helium Loop Piping Material Selection

As opposed to the corrosion issue of molten salt flows, the ideally pure helium flow does not necessarily address the corrosive concerns. The considerations of the structural materials for the helium loop mainly lie in the high temperature and high pressure. According to the facility design requirements as stated later, the helium loop will be operated under prototypic pressure range, which typically reaches around 7 MPa. Since most of the available alloy candidates have exhibited good performance in mechanical strength at elevated temperatures, intensive comparison and research are necessary.

According to Mylavarapu [7], the allowable design stress in the American Society of Mechanical Engineers (ASME) code is summarized and shown in Figure 2. It demonstrates that Alloys 230 and 617 are superior to Alloy 800H in allowable stress. This actually provides some guidelines in selection of materials for the helium loop. However, at that time when this research was carried out, neither Alloys 230 nor 617 were commercially available in the form of tube or pipe configuration. Therefore, in the HTHF at OSU, Alloy 800H was eventually selected and used as the piping material. Alloy 800H can withstand most of the stress challenges at an operation of 3 MPa and 800°C in the HTHF, whereas in this design Alloy 800H may not be able to reach 7 MPa and ~650°C (mentioned in the later chapters) at the same time. In sum, the selection of the materials used in the helium loop requires further in-depth studies in the stress analysis. In the later calculation, Alloy 800H is assumed to be used for helium loop structural material.

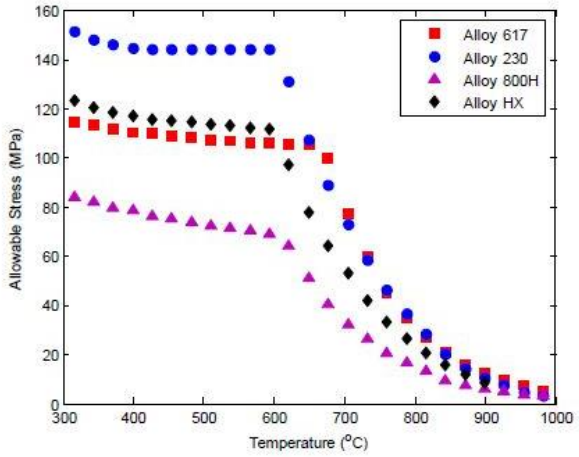

Figure 2. Allowable stress of four alloys (617, 230, 800H, and Hastelloy X) in a wide range of temperatures.

4. FACILITY DESIGN

4.1 Overview

According to the statement of work, the conceptual facility design should meet several requirements, which are outlined as follows: (1) the molten salt flow loop should satisfy several experimental testing tasks including salts heat transfer, thermodynamics and fluid-solid corrosion testing; (2) the integral facility should include a second loop for heat exchanger performance testing, which is proposed to support helium or supercritical SCO_2 flow at the prototypic pressure and temperature; (3) The fluoride molten salt loop should be capable of both forced and natural circulations for investigation of heat transfer and thermodynamic performance. These requirements have led the following conceptual design.

Figure 3 shows a 3-D model of the conceptual design. In this design, there are two flow loops coupled by a heat exchanger, which is a printed circuit heat exchanger (PCHE)-type compact heat exchanger in this case. The heat exchanger can be replaced with a shell-tube type or helical-coil type heat exchanger. The right-hand side of the facility is the fluoride molten salt (MS) loop and the left-hand side is the helium flow loop (HE). Both loops include a set of individual electrical heaters, pump (or a compressor, booster), a cooler, a corrosion test section and a heat transfer test section. The corrosion test section is parallel to the other horizontal loop section that includes a heat exchanger. It makes sure that the corrosion testing at specified elevated temperatures can be performed independently without involving the heat exchanger. The same design feature is applied to the helium flow loop. In each of the molten salt and helium loops, two heat transfer test sections are planned for both vertical and horizontal fluid flow thermal characteristics and instrumentation performance studies.

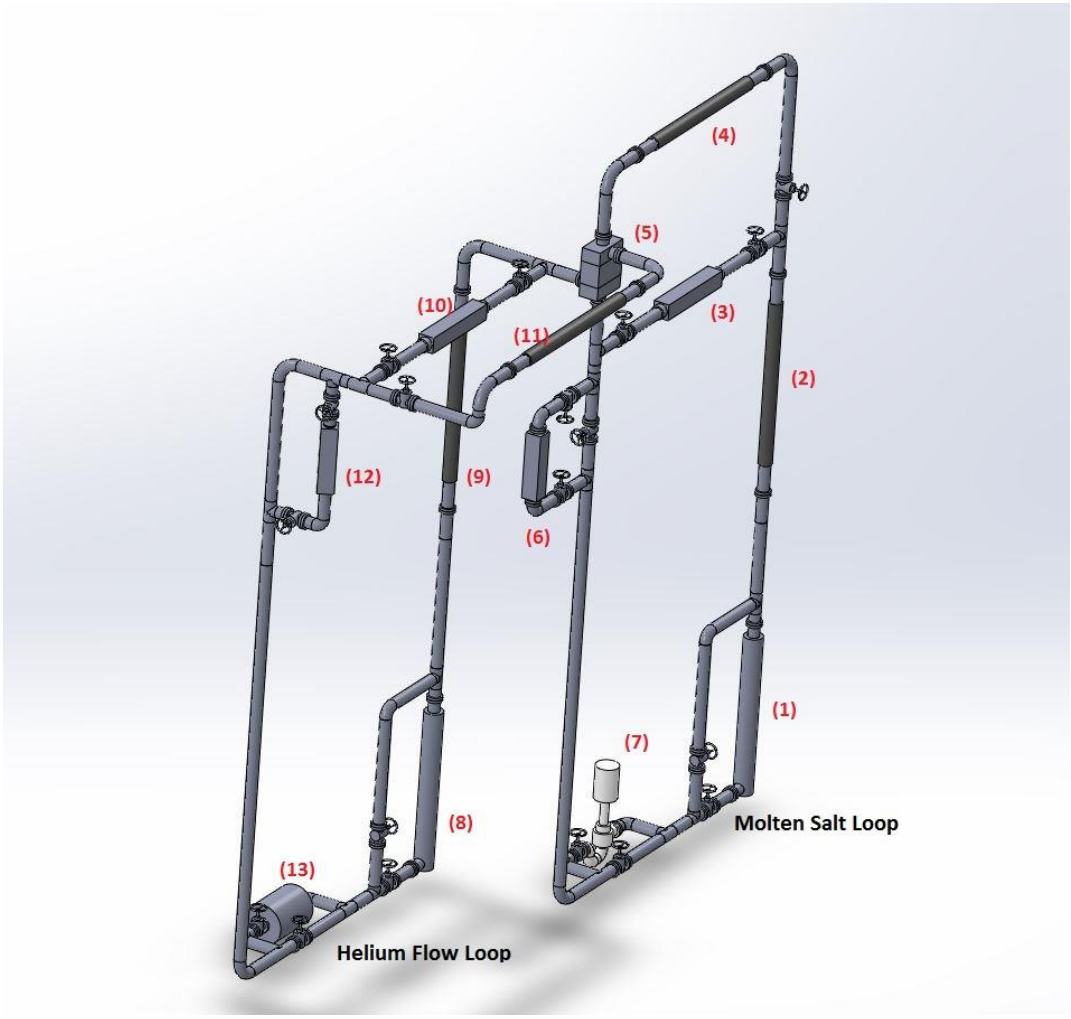

Figure 3. Schematic of the facility design: (1) molten salt (MS) heater, (2) MS vertical heat transfer test section (HTTS), (3) MS corrosion test section (CTS), (4) MS horizontal HTTS, (5) HX, (6) MS cooler, (7) pump, (8) helium (He) heater, (9) He vertical HTTS, (10) He CTS, (11) He horizontal HTTS, (12) He cooler, (13) He compressor.

Figure 4, Figure 5, and Figure 6 demonstrate the facility working features in different operational modes. Figure 4 shows the forced circulation mode in which the heat is transferred from the molten salt loop (hot side) to the helium flow loop (cold side). In the figure, arrows with the same color of the loop section indicate the direction of the flow. Red-colored loop section indicates hot flow while blue or

green-colored loop section indicates cold flow. Due to the loop being used for multi-purpose multi-fluid testing, extra flow paths in the loop are necessary to bypass certain components. The heaters in the helium flow loop, for example, are bypassed because a heat sink other than a heat source is needed in the cold side. Considering potential natural circulation application in the helium flow loop, the flow path connected with helium heater is designed to be straight, while the bypass flow line contains elbows that will increase the pressure drop. However, this could be compensated by the compressor or booster. Similar design laws are applied to the molten salt loop.

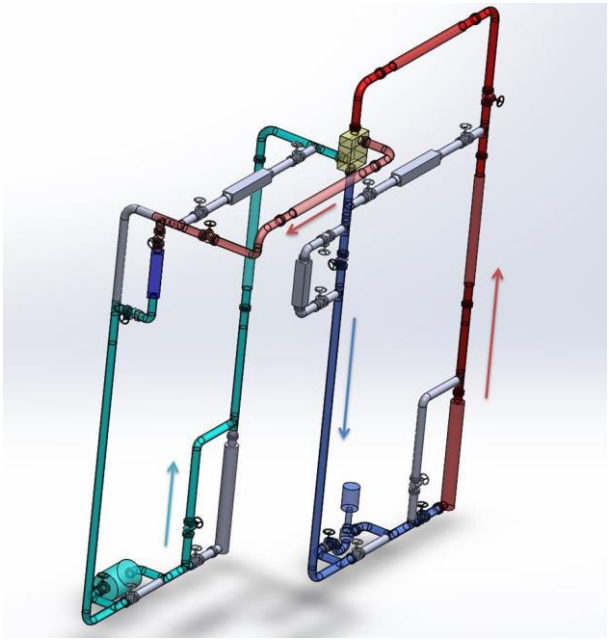

Figure 4. Schematic of the hot MS to cold He at forced circulation mode.

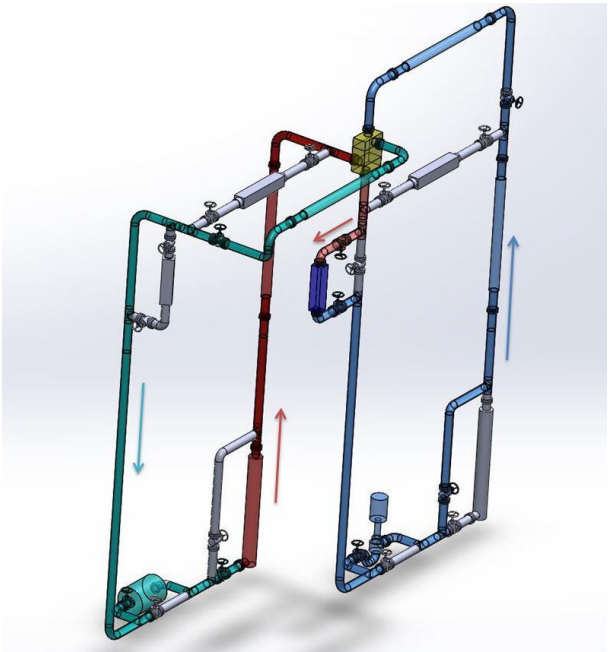

Figure 5. Schematic of the hot He to cold MS at forced circulation mode.

Figure 6. Schematic of the hot MS to cold He at natural circulation mode.

In Figure 5, the heat is reversely transferred from the helium flow loop as the hot side to the molten salt side as the cold side. In this case, the helium heaters are operated and the molten salt loop heaters are bypassed. The cooler at molten salt loop side is utilized as the heat sink to eventually dissipate the heat from the helium loop side. It is noted that the location of the cooler beneath the heat exchanger will somewhat prevent natural convection capabilities in the loop, and thus it is not ideally preferred. Usually the heat sink would be placed at higher elevations. One of the reasons for the cooler's location is that the cooler will be used for the cooling of the temperature-elevated corrosion testing. As such, the cooler must be placed downstream of the corrosion test section loop, which means it will also be placed at the downstream of the heat exchanger. Similar issues also happen to the helium cooler when the forced circulation mode is operated. The cooler position problem is perhaps negligible when forced convection modes are operated, but it might raise distortions in some thermal performances when natural circulation is of interest.

Figure 6 presents the natural circulation mode at the molten salt loop side. In this case, the molten salt loop forms a typical natural circulation loop with the heaters as the heat source and the heat exchanger as the heat sink. As stated above, all the flow paths in the natural circulation mode are intentionally designed as straight as possible to minimize pressure drop caused by extra elbows and travelled length. The helium flow loop side should be operated at forced circulation mode.

The operating conditions have been identified through reviewing the prototypic parameters proposed in Sabharwall et al. [2]. In that report, the parameters of the heat exchanger that connects secondary FLiNaK salt loop and helium Brayton cycle power conversion section have been specified as listed in Table 11. Essentially, the temperature in this design refers to that prototype of the main heater, because the facility will be tested at the prototypic temperature level in the future. The prototypic power generation is around 10 MW for each heat exchanger. From the standpoint of power scaled down to 1%, that is, the power in the model being set 100 kW, the mass flow rate of both loops can be determined. Note that fluoride molten salt selected in this design analysis is FLiNaK.

Table 11. SHX coolant information.

Prototype	Inlet-Temperature (°C)	Outlet-Temperature (°C)	Pressure (MPa)	Mass Flow Rate (kg/s)
FLiNaK	676.2	568.3	0.153	51.1
Helium	498.9	651.2	6.97	13.4
Model				
FLiNaK	676.2	568.3	0.153	0.492
Helium	498.9	651.2	6.97	0.126

The two-loop facility design has basically addressed the requirements with regard to both the economic and engineering feasibility. This chapter will unfold several parts, including the components that are used in the facility design, the thermal analysis and hydraulic analysis, etc. The whole loop analysis merely centers on the estimation of the pressure drop over pipes and heat exchanger and the heat loss over pipes.

4.2 Components Introduction

4.2.1 Heat Exchanger

Several heat exchanger concepts are proposed for studies in this facility design. Among them PCHE-type heat exchangers have been receiving much of attention for their promising characteristics in heat transfer performance, high pressure capability, and high compactness. PCHEs are also considered as a potential option for the future intermediate heat exchanger application in Very-High Temperature Reactors (VHTRs). In this facility design, PCHE is used as a reference heat exchanger for the entire loop design analysis. Figure 7 illustrates the PCHE channel cross section and configuration [7].

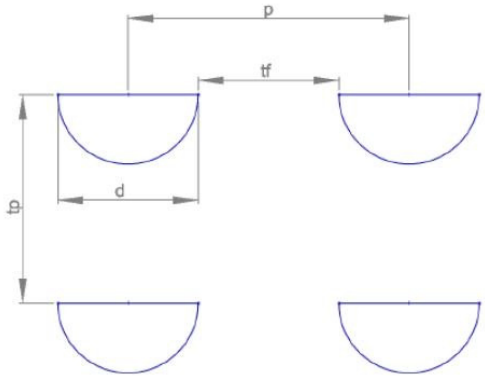

Figure 7. Illustration of PCHE channel cross section.

Table 12 shows a set of parameters of the PCHE heat exchanger geometry that is used for analyses in the design. The dimensions of the channels are based on the experience of the PCHE studies in the HTHF at OSU. Alloy 617 is chosen as the material of the PCHE.

Table 12. PCHE core model parameters [7].

Parameters	Value
Channel pitch (p), mm	2.5
Channel width (d), mm	2.0
Channel horizontal distance (t_f), mm	0.5
Plate thickness (t_p), mm	1.63
Channel hydraulic diameter ($D_{h,0}$), mm	1.22
Channel cross section (A_c), mm^2	1.57

4.2.2 Heater

Heating products to the liquids available in the commercial market generally fall into two categories: surface heating and immersion heating. Basically, the heating elements suited around pipes or vessels to heat up the liquid inside are characterized as surface heating while some of the heaters that are physically immerged in the liquid are of immersion heating. The heaters available for fluid and gas heating are (1) band heaters, (2) cable heaters, (3) cartridge heaters, (4) ceramic fiber heaters, and (5) multi-cell heaters. Ceramic fiber heaters were used for the OSU HTHF while in the (High-Temperature DRACS test Facility) HTDF, cartridge heaters will be used. There are some other types of heating elements, but they are not suitable for the application in this design. Considering the natural circulation testing characteristics in the facility, the design of the heater needs to be carefully examined. A more extensive study is required for the specification of the heaters.

4.3 Thermal Hydraulic Analysis and Estimation of Heat Exchanger Design

4.3.1 Pressure Drop in Heat Exchanger

The pressure drops across the heat exchanger for both the hot and cold sides are estimated. Typically, the flow in PCHE channels will be in laminar flow region. In addition, it is expected that most of the travelled length in the helium flow loop channel virtually falls in developing flow region. By definition, internal flows are hydrodynamically fully developed when velocity profile no longer changes as a function of distance into the pipe or channel. This condition will never be realized when a variable density fluid is heated or cooled [7]. The correlation to estimate the entrance length in laminar flow is available from Mylavarapu [9].

$$L_m = 0.06\,\mathrm{Re}\cdot D_h \tag{3}$$

L_m denotes the entrance length. The coefficient slightly varies from different studies. The channel length L_0 is given in the later thermal analysis (in Chapter 5.4), which is 0.170 m for both MS and He loops. It is calculated that $L_{m,He}$ is equal to 0.147 m, which accounts for a large portion of the travelled length L_0 of the channel. That means the whole helium flow nearly falls in hydrodynamically developing flow region. Mylavarapu [9] suggests the tabulated parameters for calculating the pressure drop over developing flow region in semi-circular channel (Table 13). It lists the $f_{app}Re$ values as a function of dimensionless z^+, which accounts for the length from the entrance to the location of interest. f_{app} denotes the apparent fanning factor, defined as:

$$f_{app} = \frac{\Delta p}{\frac{1}{2}\rho \bar{u}^2}\cdot\frac{D_h}{4z} \tag{4}$$

And z^+ is defined as:

$$z^+ = \frac{z}{\mathrm{Re}\, D_h} \tag{5}$$

Using the helium density at the mean value of the inlet and outlet temperatures, the pressure drop at developing flow region can be calculated as $\Delta p_{He,1}$ = 2720.2 Pa, while the pressure drop for the "developed region" is $\Delta p_{He,2}$ = 327.5 Pa. For the molten salt side, the same correlation could be applied. Then $L_{m,MS}$ value of 5.42 mm indicates that the developing flow region only accounts for 3.19% of the entire channel length. Accordingly, the developing flow pressure drop is negligible, and the pressure drop due to fully developed laminar flow in semicircular channel can be computed by:

$$f' = \frac{15.78}{\mathrm{Re}} \tag{6a}$$

$$\Delta p = 4 f' \frac{L_0}{D_h} \frac{\rho \bar{u}^2}{2} \tag{6b}$$

Then the pressure drop on the molten salt loop side is 1927.8 Pa. If we assume the pipe length is 4×3 m for each loop (assume the loop shape is similar to a square), the summation of the pressure drop over pipes and the heat changer can be obtained. The preliminary calculation results have shown that at molten salt coolant side the overall pressure drop is 1971.4 Pa, whereas at helium coolant side it is 8443.9 Pa.

Table 13. Flow parameters for hydrodynamically developing flow in a semi-circular duct.

z^+	f_{app}Re	z^+	f_{app}Re	z^+	f_{app}Re	z^+	f_{app}Re
0	0	0.00375	56.75	0.03	26.68	0.065	20.84
0.00025	193.12	0.005	50.62	0.04	23.54	0.074	20.25
0.0005	153.31	0.0075	42.65	0.05	22.18	0.078	20.02
0.00075	117.64	0.01	37.95	0.055	21.68	0.082	19.82
0.001	106.97	0.0125	35.07	0.060	21.21	0.123	18.49
0.00125	92.79	0.0175	30.85	0.062	21.01	0.164	17.81
0.0025	68.93	0.025	21.21	0.064	20.91		

4.3.2 Thermal Analysis in Heat Exchanger

Using the model dimension of the PCHE-type heat exchanger core (Figure 7), we could obtain the mass flow rate for both flow loops. With the assumption that Reynolds number in the heat exchanger flow channel on the helium side is 2000, the total number of channels can be determined by:

$$\mathrm{Re}_{He} = \frac{\dot{m}_{He} D_{h,He}}{A_{c,He} \mu_{He}}, \mathrm{Re}_{He,0} = \frac{\dot{m}_{He,0} D_{h,He,0}}{A_{c,He,0} \mu_{He,0}} \tag{7a}$$

$$N = \frac{\dot{m}_{He}}{\dot{m}_{He,0}} \tag{7b}$$

The subscript *0* means the mass flow rate in the semi-circular channel. In practice, the total number of channels is limited by manufacturing techniques and engineering consideration. The mass flow rate in the channel for the molten salt loop side can be determined once the total number of channels is known. With

the temperatures of the inlet and outlet in both sides known, the channel length can be estimated through Equations (8) to (10)

$$\dot{Q} = U_r A_t \Delta T_m \tag{8}$$

$$\frac{1}{U_r} = \frac{1}{h_{MS}} + \frac{\Delta t_w}{k_w} + \frac{1}{h_{He}} \tag{9}$$

$$A_t = N \cdot \xi \cdot L_0 \tag{10}$$

where $\dot{Q}$, U_r, A_t, ΔT_m, h_{MS}, Δt_w, k_w, h_{He}, ξ, L_0 are heat transfer rate, overall heat transfer coefficient, total heat transfer area, logarithmic mean temperature difference (LMTD), molten salt channel heat transfer coefficient, average plate thickness, plate conductivity, helium channel heat transfer coefficient, wetted circumference and channel travelled length, respectively. ξ is defined as:

$$\xi = \frac{4A_c}{D_{h,0}} \tag{11}$$

And ΔT_m is defined as

$$\Delta T_m = \frac{\Delta T_A - \Delta T_B}{\log\left(\frac{\Delta T_A}{\Delta T_B}\right)} \tag{12}$$

where ΔT_A and ΔT_B denote the heat exchanger inlet and outlet temperature difference between the hot and cold sides, respectively. Δt_w can be computed as recommended by Kim et al. [10] using an integral average method:

$$t_w = \frac{1}{r}\left(\int_{x=0}^{x=r} t_p - \sqrt{r^2 - x^2}\, dx\right) \tag{13}$$

With respect to the heat transfer coefficient for both the molten salts and helium flows, it is assumed that they fall in the laminar fully-developed flow region (i.e., the developing flow at the entrance region is neglected). Note that in fact the thermal analysis of the heater exchanger is performed prior to the pressure drop calculations. As is known from previous pressure drop calculation, the entrance length in helium side is significant. Therefore, the laminar fully developed assumption in the entire channel length will be conservative in heat transfer coefficient calculation. The channel length L_0 is estimated to be 0.170 m, and the overall heat transfer coefficient over the entire heat exchanger is approximately 755 W/m^2-K.

4.4 Fundamentals of Scaling Analysis

4.4.1 Scaling Laws

Assume that the heat exchanger is to be operated under the forced convection mode during testing. Thus, a 1-D governing equations can be used as follow [11][12][13]:

$$\frac{\partial}{\partial t}(\rho A)+\frac{\partial}{\partial x}(\rho u A)=0 \tag{14}$$

$$\frac{\partial}{\partial t}(\rho u A)+\frac{\partial}{\partial x}(\rho u^2 A)=-\frac{\mathrm{d}p}{\mathrm{d}x}-\frac{4\tau_w}{D_h} \tag{15}$$

$$\rho c_p \frac{\mathrm{D}T}{\mathrm{D}t}=-\nabla\cdot q''+q'''+\beta T\frac{\mathrm{D}p}{\mathrm{D}t} \tag{16}$$

$$\rho_s c_{ps}\frac{\partial T_s}{\partial t}+\nabla\cdot(k_s\nabla T_s)-\dot{q}_s=0 \tag{17}$$

$$-k_s\frac{\partial T_s}{\partial y}=h(T_s-T) \tag{18}$$

where τ_w, q'', subscript s are the wall shear stress, heat flux and for solid, respectively. These are conservation equations of mass, momentum, energy and solid energy, and boundary condition equation, respectively. Both for the molten salt and helium flow through the heat exchanger, the energy and solid energy conservation equations could be simplified to:

$$\rho c_p \frac{\mathrm{D}T}{\mathrm{D}t}=\frac{4h}{D_h}(T_s-T) \tag{19}$$

$$\rho_s c_{ps}\frac{\partial T_s}{\partial t}+\nabla\cdot(k_s\nabla T_s)=0 \tag{20}$$

Equations (14), (15), (16), (19) and (20) could be non-dimensionalized to the following forms:

$$\frac{\partial}{\partial \tau}\rho+\frac{\partial}{\partial X}(\rho U)=0 \tag{21}$$

$$\frac{\partial U}{\partial \tau}+\frac{\partial U^2}{\partial X}=\frac{1}{2}\hat{C}\frac{\mathrm{d}\hat{P}}{\mathrm{d}X}-\frac{2L_0}{D_h}f' \tag{22}$$

$$\frac{\mathrm{D}\theta}{\mathrm{D}\tau}=St(\theta-\theta_s) \tag{23}$$

$$\frac{\partial \theta_s}{\partial \tau}+\frac{\alpha_s}{\delta^2}\frac{L_0}{u_0}\hat{\nabla}^2\theta_s=0 \tag{24}$$

$$\frac{\partial \theta_s}{\partial Y} = Bi\left(\theta_s - \theta\right) \tag{25}$$

where the dimensionless numbers are defined as below:

Euler Number: $\hat{C} = \dfrac{\Delta p_0}{\frac{1}{2}\frac{G_0^2}{\rho}}$

Fanning Factor: $f' = \dfrac{\tau_w}{\frac{1}{2}\frac{G_0^2}{\rho}}$

Stanton Number: $St = \dfrac{4hL_0}{G_0 c_p D_h}$

Time Ratio Number: $\hat{T} = \dfrac{\rho\alpha_s}{\delta^2} \Big/ \dfrac{G_0}{L_0}$

Biot Number: $Bi = h\delta / k_s$

Then the similarity criteria can be obtained by setting the ratio of prototype to model of these dimensionless numbers equal to unity. From the dimensionless number ratio similarity criteria of Stanton, time ratio, and Biot number, we can derive the following ratios:

$$\delta_R = \left(\rho\alpha_s\right)_R^{1/2} \left(L_0 / G_0\right)_R^{1/2} \tag{26}$$

$$D_{h,R} = \left(\frac{\rho_s c_{ps}}{\rho c_p}\right)_R \left(\frac{\rho\alpha_s L_0}{G_0}\right)_R^{1/2} \tag{27}$$

$$h_R = k_{s,R}\left(\frac{G_0}{\rho\alpha_s L_0}\right)_R^{1/2} \tag{28}$$

where the subscript R denotes the ratio between the prototype and the scaled-down model. Meanwhile,

$$\hat{C}_R = 1, f'_R = 1 \tag{29}$$

These similarity criteria are applied to both the molten salt and helium loops, considering the compressible effect is negligible for helium flow due to the relatively small pressure drop to its system pressure. h_R is usually expressed in terms of Nusselt number. Modifying the Nusselt number ratio to substitute heat transfer coefficient in Equation (28) and combine with the hydrodynamic diameter ratio in Equation (27), we can obtain:

$$Nu_R = \left(\frac{\alpha}{\alpha_s} \frac{k_s^2}{k^2} \right)_R \tag{30}$$

Generally, the Nusselt number is dependent on Re, which is dependent on the mass flow flux G_0. Therefore, $G_{0,R}$ can be computed through the Nu ratio with sufficient information about temperature distribution and its corresponding material properties. Given the geometric similarity, L_0 is usually known due to the requirement of the facility construction, the conduction depth and hydrodynamic diameter could be computed with $G_{0,R}$. Therefore, the most important parameter in scaling analysis is $G_{0,R}$.

4.4.2 Scaling Methodology

All the scaling criteria derived above are applied to both the hot side and cold side of the heat exchanger. There is a coupled energy transfer relation between the hot and cold sides. From Equation (31) we can obtain the closure equations for four unknowns combining Equation (30) applied to both salt and helium (i.e., $G_{MS,R}$, $G_{He,R}$, $\Delta T_{MS,R}$ and $\Delta T_{He,R}$). Theoretically, these equations can generate unique solutions. However, both as one of the scaling criteria, Euler and Fanning factor ratios should be satisfied simultaneously. There should be some compromise between satisfying those criteria when searching appropriate mass flux value for the molten salt and helium.

$$\left(G_{MS} A_{MS} c_{p,MS} \Delta T_{MS} \right)_R = \left(G_{He} A_{He} c_{p,He} \Delta T_{He} \right)_R = \dot{Q}_R \tag{31}$$

It is noted that generally the inlet temperature of the hot flow and the outlet temperature of the cold flow are specified as fixed parameters due to the realistic engineering consideration, if the heat exchanger is of counter flow type. When $\Delta T_{MS,R}$ and $\Delta T_{He,R}$ are calculated from the closure equations, the outlet temperature of the hot flow and the inlet temperature of the cold flow are then determined.

The closure equations containing four unknowns are not necessarily straightforward to solve because the properties of materials both for the fluid and solid wall, are dependent on the temperature distribution within them, which still depends on the solution from the closure equations. Therefore, in this case the mass flux of the molten salt and helium should be determined through iterations. There is an implicit constraint condition in the two side coupling, where the conduction depth needs to be equal. The time scale is currently not taken into account when transient behavior is not emphasized.

5. HEAT LOSS ANALYSIS AND INSULATION SELECTION

5.1 Physical Model

The purpose of conduct heat-loss analyses is to estimate the total heat-loss rate over a section of pipe with specified length and the outmost surface temperature. Generally, a metal pipe should be covered with single or multiple layers of insulation materials to prevent great heat loss rate from high-temperature fluid flow in the pipe to the ambient environment. Thus, the physical model for heat loss analysis can be simplified to a pipe with several layers of different thicknesses as shown in the Figure 8. In this model, the fluid flows in the center region, and the first layer adjacent to flow is the pipe metal. Next to the metal layer are various kinds of insulation layers, with the outmost layer contacting ambient air.

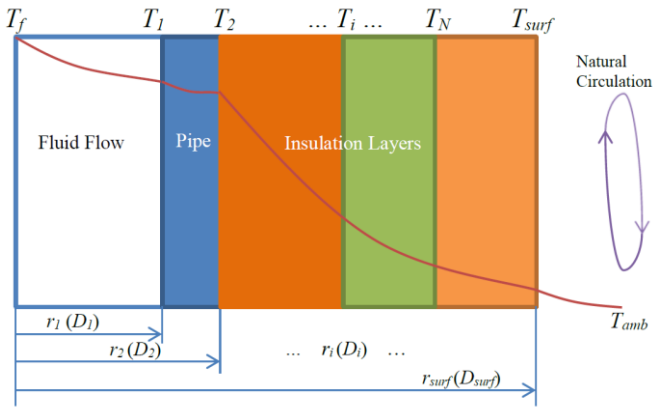

Figure 8. Schematic of insulation materials configuration.

The heat is transferred through internal forced or natural convection in the fluid flow region to the pipe metal layer. The following layers transfer heat to the outmost surface through thermal conduction. Then the heat is dissipated to the ambient environment through natural circulation. Thus, there are three thermal models available to describe the heat transfer process. Equations (32), (33), and (34) present (1) internal convection, (2) thermal conduction, (3) natural convection, where $\dot{q}'_{HL}$, T_f, T_{amb}, R_f, $T_{i,N}$, $r_{i,N}$, T_{surf}, r_{surf}, h_f, k_i, h_{nc} and R_{nc} are linear heat loss rate, fluid bulk temperature, ambient temperature, fluid flow thermal resistance, layer inner surface temperature, layer inner surface radius, outmost surface temperature, outmost surface radius, flowing fluid heat transfer coefficient to the pipe wall, average layer thermal conductivity, air natural convection heat transfer coefficient, and natural convection thermal resistance, respectively. Subscript N means N layers of insulation, except when N=1 it denotes pipe material. It is noteworthy that the radiative heat transfer at the surface is not taken into account in current analyses assuming that natural convection is predominating.

$$\dot{q}'_{HL} = 2\pi r_{1,N} h_f (T_f - T_{1,N}) = \frac{T_f - T_{1,N}}{R_f} \tag{32}$$

$$\dot{q}'_{HL} = \frac{T_{i,N} - T_{i+1,N}}{\sum_i^N \frac{\ln(r_{i+1,N} / r_{i,N})}{2\pi k_i}} \tag{33}$$

$$\dot{q}'_{HL} = 2\pi r_{surf} h_{nc} (T_{surf} - T_{amb}) = \frac{T_{surf} - T_{amb}}{R_{nc}} \tag{34}$$

From the equations above, we can simplify them into one equation as follows below:

$$\dot{q}'_{HL} = \frac{T_f - T_{amb}}{\frac{1}{2\pi r_{1,N} h_f} + \sum_i^N \frac{\ln\left(r_{i+1,N} / r_{i,N}\right)}{2\pi k_i} + \frac{1}{2\pi r_{surf} h_{nc}}} \tag{35}$$

where $T_{N+1,N} = T_{surf}$, $r_{N+1,N} = r_{surf}$.

In Equation (35) it is required to calculate h_f, k_i, h_{nc} to obtain heat loss rate value. For flowing fluid heat transfer coefficient to the pipe wall h_f, the correlations from (36), (37), (38), and (39) [1] are applied.

$$\mathrm{Nu_T} = 3.657, (\mathrm{Re} \le 2300) \tag{36}$$

$$\mathrm{Nu_H} = 4.364, (\mathrm{Re} \le 2300) \tag{37}$$

$$\mathrm{Nu} = 0.012(\mathrm{Re}^{0.87} - 280)\,\mathrm{Pr}^{0.4}, (1.5 \le \mathrm{Pr} \le 500, 3\times10^3 \le \mathrm{Re} \le 10^6) \tag{38}$$

$$\mathrm{Nu} = 0.0214(\mathrm{Re}^{0.8} - 100)\,\mathrm{Pr}^{0.4}, (0.5 \le \mathrm{Pr} \le 1.5, 10^4 \le \mathrm{Re} \le 5\times10^6) \tag{39}$$

Equations (36) and (37) are correlations for laminar flow Nusselt number calculations, where T and H denotes uniform wall temperature and uniform heat flux axially boundary conditions, respectively. Equations (38) and (39) are correlations for turbulent flow Nusselt number calculations. The calculation for transition flow in current analysis is simply interpolating a value between the laminar flow and the beginning turbulent Nusselt number (i.e., when Re = 3000).

For average layer thermal conductivity k_i, it can be calculated based on tabulated values as a function of temperature. In addition, approximate functions for thermal conductivity of different materials have been obtained as available in appendix. For air natural convection heat transfer coefficient, a relatively complicated model is used. In natural convection analyses, the geometric configuration of pipes must be considered in the model (i.e., horizontal pipes and vertical pipes). Briefly, in the case of long horizontal pipes (or circular cylinders), Nu = f(Ra), where Ra is Rayleigh number in terms of the reference temperature difference ΔT_0, which is often given as [8]:

$$\mathrm{Ra} = \frac{g\beta\Delta T_0 L^3}{\nu\alpha} \tag{40}$$

where g, β, L, ν, α are gravitational acceleration, thermal expansion coefficient, pipe length, static viscosity, and thermal diffusivity, respectively. For isoflux boundary condition, apply average temperature difference to the Equation (40) to obtain Nusselt number and then heat flux q''_{hl} at wall surface. As is known that $q''_{hl} = \dot{q}'_{HL}/(2\pi r_{surf}L)$, it is obvious that the heat loss rate can be computed when average temperature difference from wall surface to ambient temperature is known. However, from Equation (35) it is found that $\dot{q}'_{HL}$ and T_{surf} is implicitly related. Therefore, an iteration method must be applied to obtain heat loss rate as well as wall surface temperature.

In the case of long vertical pipes, there is a different physical mechanism that drives the natural convection. It is known that the local temperature difference and natural convection heat transfer coefficient vary along the pipe upward. Therefore, the Rayleigh number will be modified to either local value of Rayleigh number ($\mathrm{Ra_x}$) based on local temperature difference or value of Rayleigh number in terms of heat flux to obtain average temperature difference (Ra*), depending on the specific problem conditions, as shown in the Equation (41) [8]. For an isoflux boundary condition, the local Rayleigh number will be modified to the value in terms of uniform heat flux. Similarly, an iteration method needs to be applied to calculate heat loss rate and surface temperature simultaneously.

$$\mathrm{Ra}_x = \frac{g\beta\Delta T_0 x^3}{\nu\alpha}, \mathrm{Ra}^* = \frac{g\beta q'' L^4}{\nu\alpha k} = \mathrm{RaNu} \tag{41}$$

5.2 Methodology

An improved MATLAB code has been applied for heat loss analysis that is capable of calculating multiple insulation layers of different materials and detailed temperature distribution both radially and axially along pipes. The method used in the coding is based on thermal conduction theory. Due to the temperature dependence of the thermal conductivity of materials and air, iteration is required to adjust their thermal properties according to temperature. The temperature information is updated through each iteration in the calculation. An initial guess of temperature is based on the assumption of linear temperature drop. In addition to the thermal properties adjustment iteratively, it is necessary to discretize layer region along the radial axis in the calculation to obtain more accurate thermal conductivity values as well as radial temperature profile. Assuming radial distance of inner pipe surface to centerline as $r_{1,M}$, $r_{j,M}$ denotes the jth radial position with the entire layer region discretized into M meshes. Note $r_{M+1,M} = r_{surf}$. Correspondingly, the temperature at $r_{j,M}$ can be written into $T_{j,M}$, and similarly $T_{M+1,M} = T_{surf}$. According to one-dimensional (1-D) heat conduction in cylindrical coordinates, we have:

$$\dot{q}'_{HL} = \frac{T_{j,M} - T_{j+1,M}}{\frac{\ln\left(r_{j+1,M} / r_{j,M}\right)}{2\pi k_{j,M}}} = \frac{T_{j,M} - T_{j+1,M}}{R_{j,M}},$$
$$R_{j,M} = \frac{\ln\left(r_{j+1,M} / r_{j,M}\right)}{2\pi k_{j,M}} \tag{42}$$

where $\dot{q}'_{HL}$, $k_{j,M}$, $R_{j,M}$ are linear heat loss rate, thermal conductivity and thermal resistance in the jth mesh, respectively. Combined with Equations (43) and (44), we can obtain Equation (45) [19].

$$\dot{q}'_{HL} = 2\pi r_{1,N} h_f (T_f - T_{1,M}) = \frac{T_f - T_{1,M}}{R_f} \tag{43}$$

$$\dot{q}'_{HL} = 2\pi r_{surf} h_{nc} (T_{surf} - T_{amb}) = \frac{T_{surf} - T_{amb}}{R_{nc}} \tag{44}$$

$$\begin{cases} R_f \dot{q}'_{HL} + T_{1,M} = T_f, \\ R_{1,M} \dot{q}'_{HL} - T_{1,M} + T_{2,M} = 0, \\ R_{2,M} \dot{q}'_{HL} - T_{2,M} + T_{3,M} = 0, \\ \vdots \\ R_{j,M} \dot{q}'_{HL} - T_{j,M} + T_{j+1,M} = 0, \\ \vdots \\ R_{M-1,M} \dot{q}'_{HL} - T_{M-1,M} + T_{M,M} = 0, \\ R_{M,M} \dot{q}'_{HL} - T_{M,M} + T_{surf} = 0, \\ R_{nc} \dot{q}'_{HL} - T_{surf} = -T_{amb}. \end{cases} \tag{45}$$

where T_f is the fluid bulk temperature either at hot leg or cold leg of facility, and T_{amb} is ambient temperature which can be assumed in the calculation. In these equations it is noticed that T_f and T_{amb} need to be given as boundary condition for solving matrix equations. Then we can cast formulas into matrix shown in Equation (47) [2] to obtain the vector containing $\dot{q}'_{HL}$ and $T_{j,M}$, which are unknowns in these equations. R_f and $R_{j,M}$ can be calculated using appropriate model and updated temperature information.

However, R_{nc} (the thermal resistance of air natural convection) cannot be determined explicitly. From air natural convection model, we can conclude that T_{surf} is a function of $\dot{q}'_{HL}$, which also means R_{nc} cannot be obtained unless $\dot{q}'_{HL}$ is known because there exists a universal function:

$$R_{nc} = \frac{T_{surf} - T_{amb}}{\dot{q}'_{HL}} = \frac{f(\dot{q}'_{HL}) - T_{amb}}{\dot{q}'_{HL}} = F(\dot{q}'_{HL}) \tag{46}$$

Therefore, temperature and heat loss rate vector in the matrix can only be solved through iterations.

$$\begin{bmatrix} R_f & 1 & & & & & & & \\ R_{1,M} & -1 & 1 & & & & & & \\ R_{2,M} & & -1 & 1 & & & & & \\ \vdots & & & \ddots & \ddots & & & & \\ R_{j,M} & & & & -1 & 1 & & & \\ \vdots & & & & & \ddots & \ddots & & \\ R_{M,M} & & & & & & -1 & 1 & \\ R_{nc} & & & & & & & -1 & \end{bmatrix} \begin{bmatrix} \dot{q}'_{HL} \\ T_{1,M} \\ T_{2,M} \\ \vdots \\ T_{j,\mathrm{M}} \\ \vdots \\ T_{M,M} \\ T_{surf} \end{bmatrix} = \begin{bmatrix} T_f \\ 0 \\ 0 \\ \vdots \\ 0 \\ \vdots \\ 0 \\ -T_{amb} \end{bmatrix} \tag{47}$$

5.3 Insulation Selection

To address heat loss rate problem, one of the most important issues is the appropriate selection of insulation material, so that the heat loss analysis can be carried out. As is observed, in the above equations $R_{j,M}$ is determined based on insulation material selected. To select appropriate insulation material, several criteria have been set according to the literature and industrial guidelines. Factors affecting final selection include the locations and parts of the piping system to be insulated (for example, inside or outside, pipes or valves), thermal requirements (high temperature or high heat loss rate), life span of insulation, corrosion concern (corrosion under insulation [CUI]), health and safety concern (whether touchable outmost surface temperature is required), and chemical resistance [20]. Insulation materials and thickness requirements for a high-temperature test section of helium loop and for steam line piping can differ greatly with each other.

The purpose of insulation material selection in the multi-fluid facility are generalized to pursue (1) high temperature resistance (up to 720°C), (2) low heat loss, and (3) relative low economic cost. Therefore, among hundreds of various insulation materials, several categories have been taken into consideration, which are:

1. Mineral fiber
2. Calcium silicate
3. Molded expanded perlite
4. Silica aerogel
5. Microporous insulation.

These materials' characteristics have been summarized in

Table 14.

Table 14. Summary of different insulation materials' characteristics.

Insulation Material	Operating Temperature Limit (°C)	Thermal Conductivity at Typical Temperature (W/m-°C)
Mineral Fibers	650	0.094 (370°C)
Calcium Silicate	650	0.096 (370°C)
Molded Expanded Perlite	650	0.114 (370°C)
Silicate Aerogel Blankets	650	~0.09 (650°C)
Microporous Insulation	1000	~0.03 (650°C)

Figure 9. Mineral fibers, calcium silicate and molded perlite (from left to right).

Mineral fiber is defined as an insulation composed principally of fibers manufactured from rock, slag, or glass with or without binders. In this category, two products are included which are fiberglass and mineral wool. They are actually both specified in the same code American Society for Testing Materials (ASTM) C 457 [21]. The highest temperature they can withstand is around 760°C. Typical products are MinWool-1200 [22] from Industrial Insulation Group, LLC (IIG). Its operating temperature limit goes up to 650°C, and the average thermal conductivity at 370°C is as low as 0.094 W/m-°C. It is easily for installation, and can even be directly installed on pipes without shutting down operation. It is especially applicable to most parts of the INL facility except the high-temperature test section in the helium flow loop.

Calcium silicate is defined as an insulation composed mainly of hydrous calcium silicate, and usually contains reinforcing fibers. Its pipe products are usually supplied as hollow cylinder shapes split in half lengthwise or as curved segments. It is specified in ASTM C 533 [23]. Typically, it inhibits corrosion on carbon steel and stainless steel piping and equipment. Thermo-12 Gold from IIG [22] is one of this kind of insulation, with operating temperatures reaching up to 650°C. Its thermal conductivity at 370°C is around 0.096 W/m-°C. It is also stated to be fire-proof. Similarly, it can also be applicable to most parts of the INL facility except the high-temperature test section in the helium flow loop.

Molded expanded perlite is an insulation composed mainly of expanded perlite and silicate binders, and may contain reinforcing fibers. It is specified in ASTM C 610 [24]. Like calcium silicate, it is also supplied as hollow cylinder shapes split in half lengthwise or as curved segments. Typically it can withstand high temperatures up to 650°C, and its thermal conductivity at 370°C is as low as 0.114 W/m-°C. Sproule WR-1200 is one of this kind from IIG [22]. Like the insulation materials mentioned above, it can be used in most situations except the high-temperature test section in the helium flow loop.

These traditional insulation materials have similar characteristics in high-temperature resistance and thermal conductivities at elevated temperatures. One of the big differences among them is probably that calcium silicate has a higher compressive-resistance and flexural-strength values than mineral fiber. And most of calcium silicate and perlite insulation are non-combustible. All of them may have relatively high thermal conductivity at high temperatures.

In addition, two advanced insulation material have been developed in the past decades, aerogel flexible blankets and microporous insulation. The aerogel blanket is a composite of an amorphous silica-based aerogel, a fibrous carrying media or reinforcements, or a combination thereof, that allow the construction to be flexible. It is specified in ASTM C 1728 [25]. The primary advantages of this material are super-low thermal conductivity at high temperatures (around 0.09 W/m-°C at 650°C) and flexibility. It is usually installed by spiral wrapping around pipes multiple times to get desired thickness. The available products are Pyrogel XT-E from Aspen Aerogels and reach 650°C as the limiting temperature. This product is also used in the HTHF at OSU. Though no corrosion inhibitors are contained in Pyrogel, it is stated no CUI will occur [26]. Another kind of advanced insulation material is microporous insulation. Microporous insulation is comprised of compacted inorganic metal oxide powders of surface area greater than 90 m^2/g, powdered inorganic infra-red opacifiers and man-made or natural fibers or filaments. It is specified in ASTM C 1676 [27]. This material is characterized by the extremely low thermal conductivity at elevated temperatures (0.03 W/m-°C at 650°C). It is actually widely used in the industry where high-temperature resistance is needed with minimum thickness and weight. Its operating temperature limit reaches around 1000°C [28]. It is one of the most desirable insulation materials for the high-temperature test section of the helium flow loop. Currently at OSU we are interested in Microtherm Moulded Products from Microtherm. It can be one of the insulation candidates for the in molten salt loop.

In summary, traditional insulation material are suitable for most thermal insulation conditions in the INL facility in terms of operating temperatures withstanding, while aerogel blankets and microporous insulation provide excellent solutions for the insulation of high-temperature sections. Therefore, work is needed to identify insulation requirement for different parts of the facility, and multiple layers of different materials (for example, two different insulation materials will be practical) can be applied using the MATLAB code as an assisting tool, which will be preliminarily discussed in the later section. Finally, the total cost should be calculated for economy consideration, including installation cost, metal jacket cost, other piping components, insulation solutions, and maintenance.

5.4 Heat Loss Analysis Cases Studies

5.4.1 Case Studies for Molten Salt (MS) Loop Insulation Solution

Preliminary pipe sizing at MS loop is chosen to be NPS 2.5 ft SCH 40 Inconel 600 pipe. This pipe size is only for the presentation of cases studies, and is required for detailed and in-depth discussion to determine the final pipe size. In the MS insulation cases studies we include five cases as a standpoint to examine the heat loss rate and insulation performance, as well as the feasibility of multiple layers of different insulation materials. First, we apply Microtherm Moulded Products from Microtherm as insulation material for both hot leg and cold leg insulation at MS loop. Three cases have been carried out using the MATLAB code to determine the appropriate insulation thickness. Another case takes into account the two different material layers as comparison to the former three cases. The last one is only considering the second type of insulation material as the entire insulation material for the bare pipe, which in this case is chosen to be MinWool-1200 (MW) from IIG. The geometric dimensions of pipe and insulation layers for these five cases are displayed in the Table 15. In the table, the description gives basic information of the insulation configuration. For example, 'NPS 2.5 ft SCH 40, MT 1.5 ft, OD. 6.62 ft means Inconel 600 pipe size is 2.5 ft, schedule 40, insulated with Microtherm Moulded Products (MT) thickness 1.5 in., and outmost diameter (OD.) is 6.62 in. MW denotes MinWool-1200 product. It is important to note that the selection of insulation thickness is not arbitrary. It is based on the dimension of standard pipe and tubing insulation [29]. As to standard product dimension of microporous insulation, the commercially available insulation thickness is always 1 in. [27], which means Case I presents imaginary conditions, only serving to demonstrate the heat loss analysis compared with other cases. Additionally, D_i and r_i are diameter and radius of multiple layers. Figure 8 gives a schematic of the insulation configuration for these cases, as described in the physical model discussion.

Table 15. Geometries of the cases for molten salt loop heat loss analysis and insulation selection.

Case No.	Description	D_1 / r_1 (mm)	D_2 / r_2 (mm)	D_3 / r_3 (mm)	D_4 / r_4 (mm)
I	NPS 2.5 ft SCH 40, MT 1.5 ft, OD. 6.62 ft	62.718 / 31.359	73.03 / 36.515	168.15 / 84.075	N/A
II	NPS 2.5 ft SCH 40, MT 2 ft, OD. 7.62 ft	62.718 / 31.359	73.03 / 36.515	193.55 / 96.775	N/A
III	NPS 2.5 ft SCH 40, MT 1 ft, OD. 5 ft	62.718 / 31.359	73.03 / 36.515	127.00 / 63.50	N/A
IV	NPS 2.5 ft SCH 40, MT 1 ft, MW 1 ft, OD. 7.62 ft	62.718 / 31.359	73.03 / 36.515	127.00 / 63.50	193.55 / 96.775
V	NPS 2.5 ft SCH 40, MW 2.5 ft, OD. 8.62 ft	62.718 / 31.359	73.03 / 36.515	193.55 / 96.775	N/A

The relevant parameters as boundary conditions in the calculations are in accordance with those given by INL, as summarized in Table 16. In addition, it is assumed that ambient temperature is 30°C, maximum allowable touch temperature is 60°C, and horizontal and vertical pipes are both 3 m long, which are also detailed in Table 16.

Table 16. Parameters used in the MS case studies.

Terms	Values	Description
$T_{MS,CL}$	430°C	MS Loop Cold Leg Temperature
$T_{MS,HL}$	480°C	MS Loop Hot Leg Temperature
T_{amb}	30°C	Ambient Temperature
P_L	52.6 kW	Heat Power Load
N_{Mesh}	100	Number of Meshes for Calculation
L_{horz}	3 m	Horizontal Pipe Length in Calculation
L_{vert}	3 m	Vertical Pipe Length in Calculation
$T_{surf,allowable}$	60°C	Allowable Surface Temperature

According to power load 52.6 kW, the mass flow rate at MS loop is calculated as 1.0057 kg/s, which is matched with the value provided by INL. The physical properties of molten salt KF-ZrF_4 is based on suggested functions as shown in appendix. The thermal conductivity as a function of temperature is obtained using commercial polynomial fitting software *CurveExpert* [30]. The data are available from commercial products' technical datasheet.

Table 17 summarizes the result of calculation analysis. It is observed that in the Case II, the surface temperatures generally meet the maximum touchable temperature requirement, but linear heat loss rate is the smallest among all five cases. It is interesting to know that Case IV shows similar characteristics compared with Case II. It indicates that the two-layer insulation solution is practical and equivalent to single insulation material. Figure 10, Figure 11, and Figure 12 show the radial temperature distribution in the layers including pipe materials. Figure 12 particularly demonstrates the similar characteristics of insulation of Case II and Case IV. Then it is strongly believed that in the application of MS loop the two-layer insulation solution with relatively low and high-thermal-conductivity materials combination may generate satisfying performance in heat loss insulation. However, the assumption made in the calculation may be subject to change, and the calculation does not address fluid bulk temperature drop along the pipe. (The assumption that fluid bulk temperature does not greatly vary along pipe axis has been

confirmed true using MATLAB code; however, for vertical pipe, the surface temperature can be truly affected by using local natural convection heat transfer coefficient instead of average value.) Furthermore, the gap between the insulation and pipe and two different insulations may probably affect the accuracy of the calculation results. Therefore, more studies emphasizing the realistic conditions and constraints will be conducted in the future.

Table 17. Summary of calculation MS cases results.

	Hot Leg		**Cold Leg**	
MS CASE I	**Horizontal**	**Vertical**	**Horizontal**	**Vertical**
$\dot{q}'_{HL}$ (W/m)	69.94	68.26	61.28	59.76
T_{surf} (°C)	62.7	72.4	59.4	68.2
h_{nc} (W/m^2-°C)	4.05	3.05	3.94	2.96
	Hot Leg		**Cold Leg**	
MS CASE II	**Horizontal**	**Vertical**	**Horizontal**	**Vertical**
$\dot{q}'_{HL}$ (W/m)	60.99	59.83	53.47	52.42
T_{surf} (°C)	56.7	64.4	54.0	61.0
h_{nc} (W/m^2-°C)	3.76	2.86	3.66	2.78
	Hot Leg		**Cold Leg**	
MS CASE III	**Horizontal**	**Vertical**	**Horizontal**	**Vertical**
$\dot{q}'_{HL}$ (W/m)	99.45	95.36	86.99	83.32
T_{surf} (°C)	82.3	98.5	76.9	91.4
h_{nc} (W/m^2-°C)	4.77	3.49	4.65	3.40
	Hot Leg		**Cold Leg**	
MS CASE IV	**Horizontal**	**Vertical**	**Horizontal**	**Vertical**
$\dot{q}'_{HL}$ (W/m)	75.05	73.89	65.12	64.06
T_{surf} (°C)	61.4	70.6	58.1	66.3
h_{nc} (W/m^2-°C)	3.93	2.99	3.81	2.90
	Hot Leg		**Cold Leg**	
MS CASE V	**Horizontal**	**Vertical**	**Horizontal**	**Vertical**
$\dot{q}'_{HL}$ (W/m)	152.24	149.42	125.14	122.81
T_{surf} (°C)	80.6	94.6	73.3	85.2
h_{nc} (W/m^2-°C)	4.38	3.37	4.21	3.23

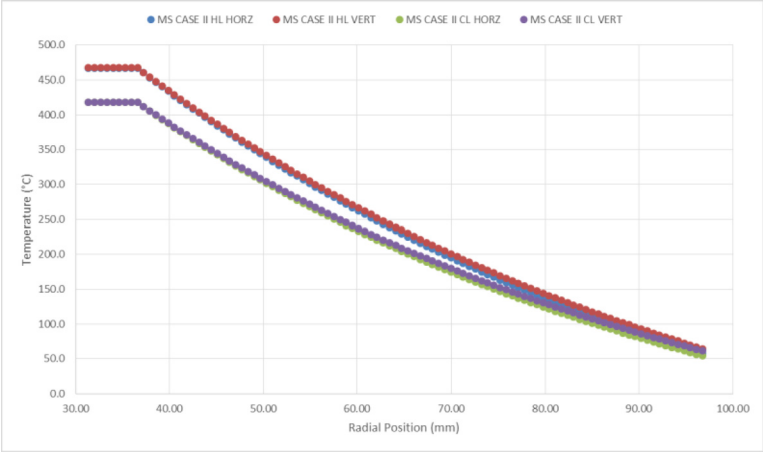

Figure 10. Radial temperature distribution in the MS Case II.

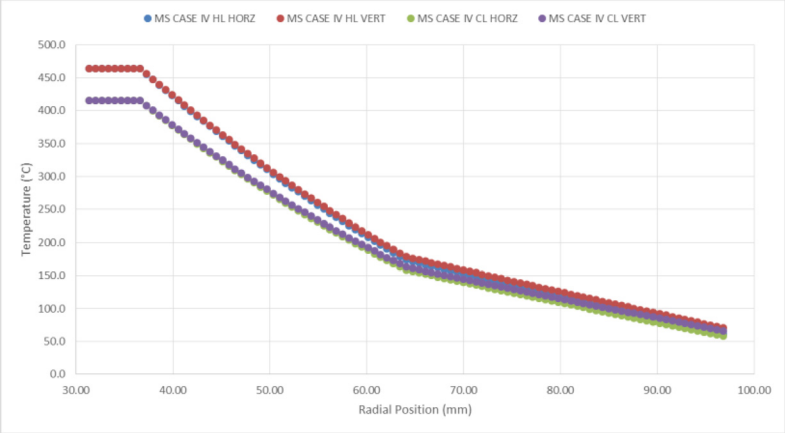

Figure 11. Radial temperature distribution in the MS Case IV.

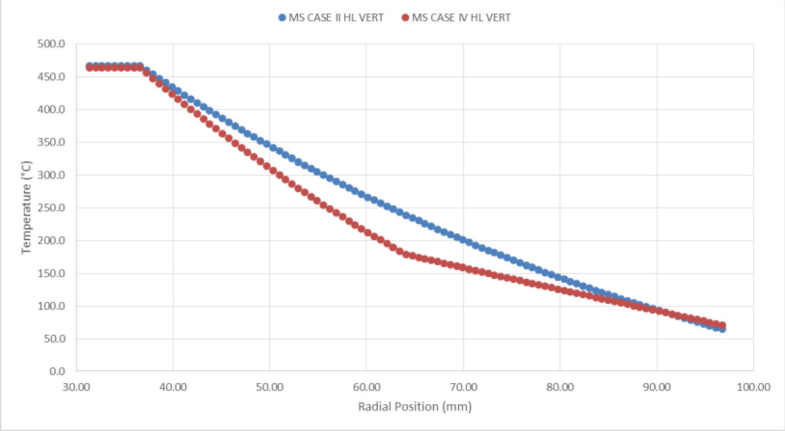

Figure 12. Hot leg vertical pipe radial temperature distribution comparison between MS Case II and IV.

5.4.2 Case Studies for Helium Flow (He) Loop Insulation Solution

The pipe size in the He loop cases studies has been chosen to be either NPS 1.5 ft SCH 160 or NPS 2 ft SCH 160, as discussed later in the next section. In this section, 1.5 ft SCH 160 Incoloy 800H has been used for four cases studies. Similar to MS insulation calculation, these cases are analyzed by MATLAB code to examine the heat loss rate and seek appropriate insulation thickness. For the helium flow loop, large temperature differences exist between hot leg and cold leg, thus different insulation solution may be considered. The geometric dimensions of four cases are summarized in Table 18. The first case uses entire Microtherm MT product as insulation material, with 3 in. thick at hot leg and 2 in. thick at cold leg. The following cases analyze multiple-insulation-layer solution. Case II uses MinWool-1200 (MW) as outmost insulation material. Case III and IV use Pyrogel-XT from Aspen Aerogels (Pyrgl) as outmost insulation material. This product is characterized by its flexibility, thus it can be wrapped on the pipe and insulation in practice to get desired thickness, usually in units of mm. Case III and IV are essentially the same. The purpose of specifying different MT thickness in these two cases is to find the smaller diameter of insulation layer. It is noteworthy that because of the large temperature difference between hot and cold legs, the specification of insulation dimension applied to these parts of pipes will be different as shown in Table 18.

Table 18. Geometric dimensions of the cases for helium flow loop heat loss analysis and insulation thickness selection.

Case No.	Part of Pipe	Description	D_1 / r_1 (mm)	D_2 / r_2 (mm)	D_3 / r_3 (mm)	D_4 / r_4 (mm)
I	Hot Leg	NPS 1.5 ft SCH 160, MT 3 ft, OD. 8.62 ft	33.986 / 16.993	48.26 / 24.13	218.95 / 109.47	N/A
	Cold Leg	NPS 1.5 ft SCH 160, MT 2 ft, OD. 6.62 ft	33.986 / 16.993	48.26 / 24.13	168.15 / 84.07	N/A
II	Hot Leg	NPS 1.5 ft SCH 160, MT 2 ft, MW 1 ft, OD. 8.62 ft	33.986 / 16.993	48.26 / 24.13	168.15 / 84.07	218.95 / 109.47
	Cold Leg	NPS 1.5 ft SCH 160, MT 1 ft, MW 1 ft, OD. 6.62 ft	33.986 / 16.993	48.26 / 24.13	101.6 / 50.8	168.15 / 84.07
III	Hot Leg	NPS 1.5 ft SCH 160, MT 1 ft, Pyrgl 50, OD. 201.6	33.986 / 16.993	48.26 / 24.13	101.6 / 50.8	201.6 / 100.8
	Cold Leg	NPS 1.5 ft SCH 160, MT 1 ft, Pyrgl 30, OD. 161.6	33.986 / 16.993	48.26 / 24.13	101.6 / 50.8	161.6 / 80.8
IV	Hot Leg	NPS 1.5 ft SCH 160, MT 2 ft, Pyrgl 15, OD. 198.15	33.986 / 16.993	48.26 / 24.13	127.00 / 63.50	198.15/ 99.07
	Cold Leg	NPS 1.5 ft SCH 160, MT 2 ft, Pyrgl 10, OD. 188.15	33.986 / 16.993	48.26 / 24.13	168.15 / 84.07	188.15 / 94.07

Other relevant parameters are listed in Table 19, with maximum allowable temperature at hot leg being 100°C. This is certainly reasonable because it is not necessary to use very thick insulation to shield the extremely-high-temperature pipe, which may also create a large economic burden [20]. However, at cold leg with relative low temperature, 60°C requirement is necessarily valid.

The helium mass flow rate is calculated to be 0.0338, similar to the parameter given by INL. The physical property function as temperature is obtained through *CurveExpert* [30]. Also the data are available through manufacturer's datasheet.

Table 19. Parameters used in the He cases studies.

Terms	Values	Description
$T_{He,CL}$	450°C	He Loop Cold Leg Temperature
$T_{He,HL}$	750°C	He Loop Hot Leg Temperature
T_{amb}	30°C	Ambient Temperature
P_L	52.6 kW	Heat Power Load
N_{Mesh}	100	Number of Meshes for Calculation
L_{horz}	3 m	Horizontal Pipe Length in Calculation
L_{vert}	3 m	Vertical Pipe Length in Calculation
$T_{surf,allowable}$	100°C	Allowable Surface Temperature

Error! Not a valid bookmark self-reference. shows the summary of calculation results. It is observed that direct use of MT insulation can provide promising performance. With the same thickness, Case II indicates that the use of MW as outer insulation instead of MT can yield similar performance and probably much lower cost. Case III and IV shows that the difference in geometric thickness of different materials does not necessarily affect greatly the insulation performance. But the latter case may require less materials, since in the Case III Pyrogel usage reaches 50 mm thick (around 2 in.), whereas in the Case IV only 15 mm thick Pyrogel is needed.

Table 20. Summary of calculation He cases results.

MS CASE I	**Hot Leg**		**Cold Leg**	
	Horizontal	**Vertical**	**Horizontal**	**Vertical**
$\dot{q}'_{HL}$ (W/m)	73.77	72.95	46.02	45.14
T_{surf} (°C)	58.5	66.7	53.4	60.6
h_{nc} (W/m^2-°C)	3.77	2.89	3.72	2.79
MS CASE II	**Hot Leg**		**Cold Leg**	
	Horizontal	**Vertical**	**Horizontal**	**Vertical**
$\dot{q}'_{HL}$ (W/m)	79.62	78.93	55.84	54.97
T_{surf} (°C)	60.2	69.0	57.3	65.8
h_{nc} (W/m^2-°C)	3.83	2.94	3.87	2.91
MS CASE III	**Hot Leg**		**Cold Leg**	
	Horizontal	**Vertical**	**Horizontal**	**Vertical**
$\dot{q}'_{HL}$ (W/m)	88.38	87.68	49.17	48.38
T_{surf} (°C)	64.8	75.1	55.3	63.3
h_{nc} (W/m^2-°C)	4.01	3.07	3.82	2.86
MS CASE IV	**Hot Leg**		**Cold Leg**	
	Horizontal	**Vertical**	**Horizontal**	**Vertical**
$\dot{q}'_{HL}$ (W/m)	78.78	77.95	42.70	42.05
T_{surf} (°C)	62.1	71.6	50.5	56.7
h_{nc} (W/m^2-°C)	3.94	3.01	3.52	2.67

Figure 15a, and Figure 15b show the radial temperature distribution of Case I and IV and comparison in terms of temperature distribution on vertical hot leg pipes. Figure 15b shows the detailed temperature distribution information among four cases. We can make a conclusion that all of the solutions ensure the surface temperature below requirement, but Case IV probably cost the least because of less materials used for insulation. Using the method specified above and MATLAB code developed in OSU, many insulation solutions can be investigated to seek the optimum design of pipe insulation. Both MS and He insulation calculations indicate that the combination of different insulation materials may cost less than the usage of single products. Additionally, from both calculations we know that horizontal pipes display better natural convection heat transfer than vertical pipes. It is possible that extra thickness of insulation on vertical pipe can somehow decrease surface temperature.

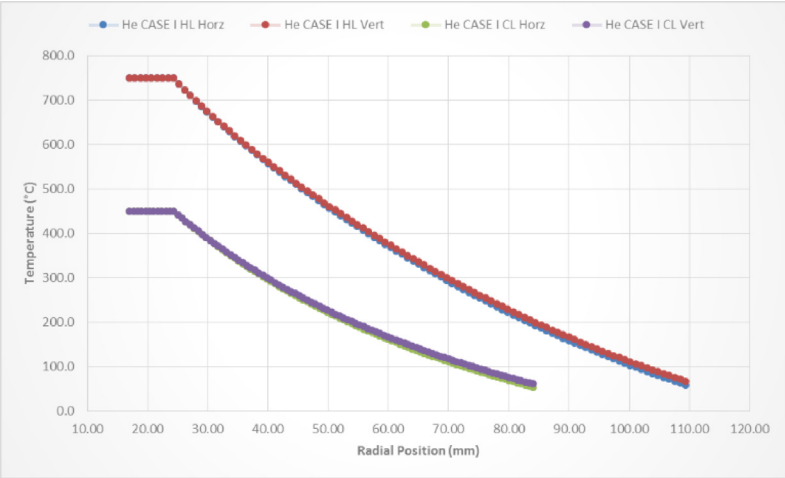

Figure 13. Radial temperature distribution in the He Case I.

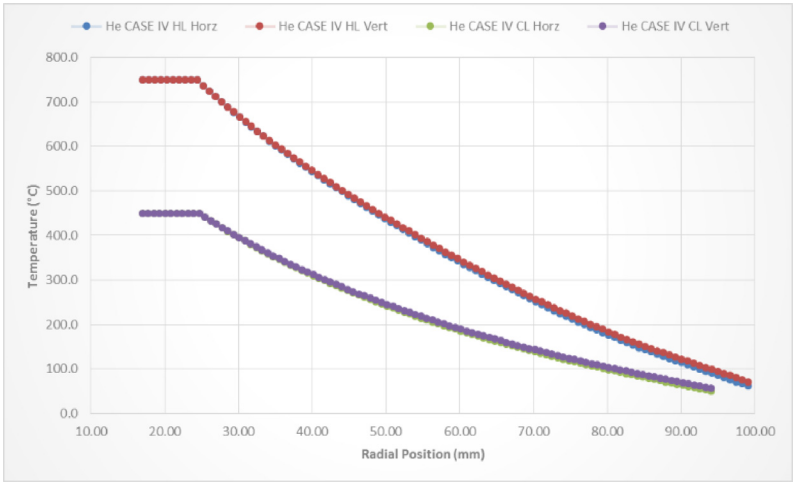

Figure 14. Radial temperature distribution in the He Case IV.

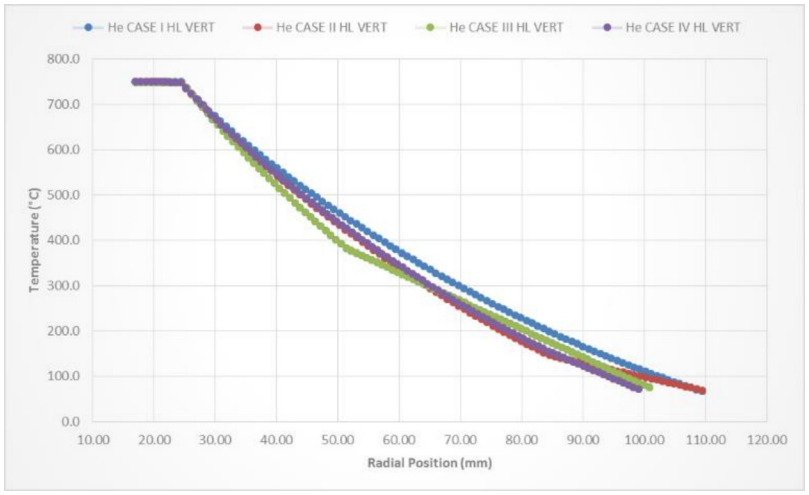

Figure 15a. Hot leg vertical pipe radial temperature distribution comparison among He cases.

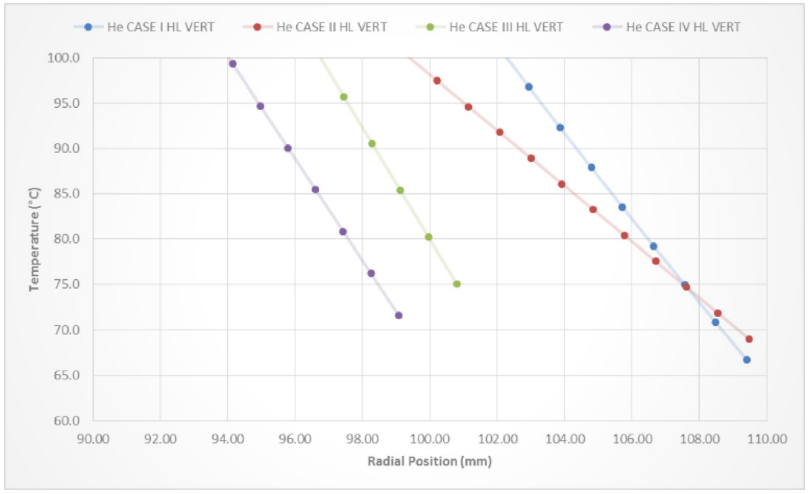

Figure 15b. Hot leg vertical pipe radial temperature distribution comparison below 100°C.

6. PRESSURE RATING AND PIPE SIZING

6.1 Pressure Rating

As stated in the ASME B31.3 [31] (ASME code for Process Piping), the required thickness of straight sections of pipe have been suggested in accordance with Equation (48)

$$t_m = t + c \tag{48}$$

The minimum thickness for the pipe selected should not be less than t_m. t_m is the minimum required thickness including mechanical, corrosion and erosion allowance. t is the pressure design thickness as calculated in Equation (49a). c is the sum of mechanical allowances. Equation (49b) presents the determination of the pipe thickness under internal pressure:

$$t = \frac{PD}{2(SE + PY)} \tag{49a}$$

$$t = \frac{P(d+2c)}{2[SE - P(1-Y)]} \tag{49b}$$

where *P, D, S, E, Y, d* are internal design gage pressure, outside diameter of pipe, quality factor, maximum allowable stress with varying temperature and coefficient from either the table listed in ASME B31.3 or additional expression based on the relation of the thickness and outer pipe diameter, respectively. It is noteworthy that *P* and *S* should be in the same unit either MPa or psi; *E* is typically equal to 1 for seamless pipe; *Y* is a coefficient to account for the non-linear reduction in allowable stress at design temperature above 482°C; and *d* is the inside diameters of the pipe, which should be the maximum value allowable under the purchase specification in the pressure design calculation. The values are valid for $t < D/6$, and interpolation for intermediate temperatures is advised. For $t \geq D/6$, *Y* is calculated by Equation (50**Error! Reference source not found.**):

$$Y = \frac{d+2c}{D+d+2c} \tag{50}$$

c is usually taken as 1 mm **Error! Reference source not found.**. For the pressure rating calculations, quation (49b) can be modified to the form shown below:

$$P = \frac{2tSE}{D-2tY} \tag{51a}$$

$$P = \frac{2tSE}{d+2c+2t(1-Y)} \tag{51b}$$

It is required that the internal pressure design thickness for straight pipe should not be less than that calculated from Equation (49a), (49b). Therefore, the internal gage pressure should not be greater than that calculated from Equation (51a), (51b). If it is assumed that *d* is calculated based on the expression (52**Error! Reference source not found.**):

$$d = D - 2t_m = D - 2(t+c) \tag{52}$$

Then (51a) and (51b) are essentially identical. Figure 16 shows the maximum allowable stress for Alloy 800H and SS 316 as listed in the ASME code. Based on the data of allowable stress, three cases of 800H pipe size and five cases of SS 316 pipe size have been analyzed for pressure-temperature ratings. Partial data for the maximum allowable operational pressure based on Equation (51a), (51b) are listed in the Table 21 and Table 22. The pressure-temperature ratings are demonstrated in Figure 17 and Figure 18. It indicates that both 2 ft SCH 160 and 1.5 ft SCH 160 pipes can withstand 7 MPa at 720°C, and all pipes except 2 ft SCH 40 can meet the requirements of steam line (15 MPa at 350°C).

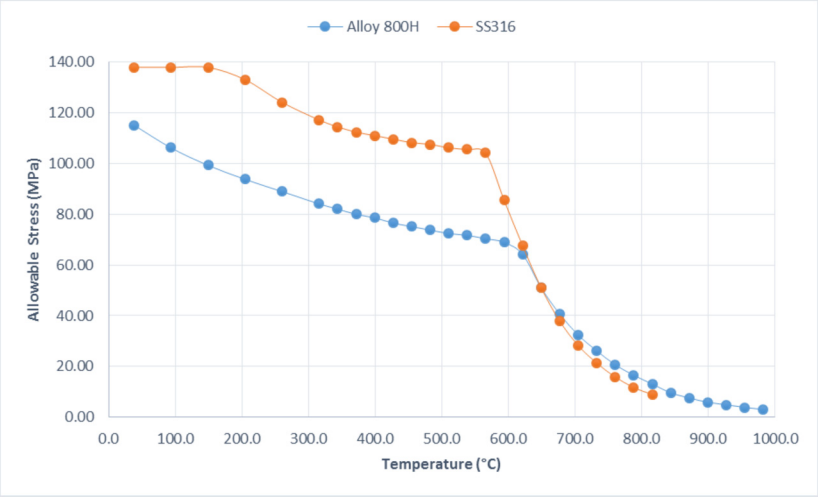

Figure 16. Maximum allowable stress for Alloy 800H and SS 316 (in metric units).

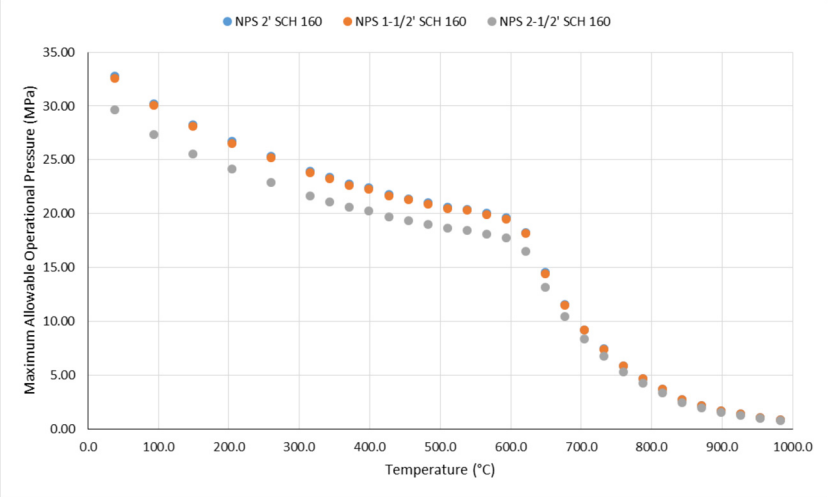

Figure 17. Pressure-temperature ratings of Alloy 800H.

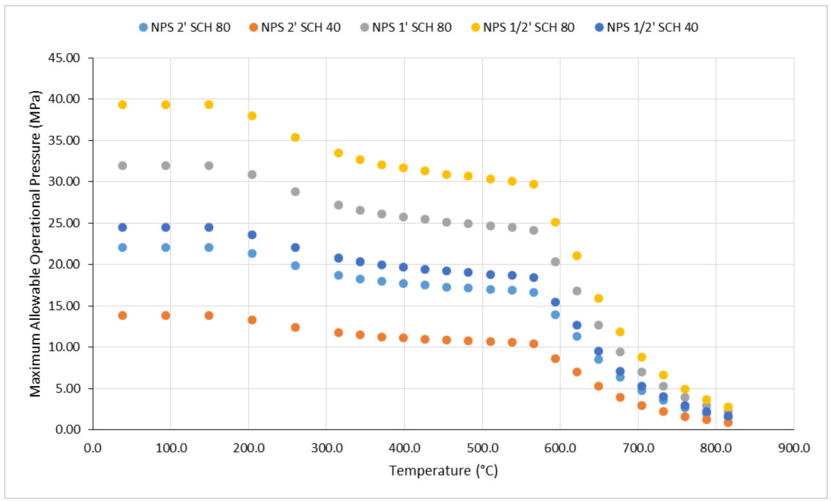

Figure 18. Pressure-temperature ratings of SS 316.

The parameters for different cases of pipe size pressure rating are shown in the Table 23. For the Alloy 800H pipes, the velocity of fluid is calculated based on the assumption that helium flows in the high-temperature test section with temperature 720°C, mass flow rate 0.0316 kg/s and density 3.367 kg/m^3. For the SS 316 pipes, first the mass flow rate is calculated as shown below:

$$\dot{m}_{Steamline} = \frac{PowerLoad}{h(350^\circ C) - h(250^\circ C)} = \frac{52.6\text{kW}}{(2693.1 - 1086.1)\text{kJ/kg}} = 0.0327\text{kg/s} \tag{53}$$

where h is the enthalpy of water or steam. Then, the velocity of steam is calculated assuming that steam flows through pipe with temperature 350°C and steam density 87.11 kg/m^3 (at 350°C). As we can observe, for the helium flow, 1.5 ft SCH 160 pipe can lead to more or less satisfactory fluid velocity, and for the steam line, pipe sizes greater than NPS 1 ft may generate fluid velocity less than 1 m/s. The fluid velocity and optimum pipe sizing will be discussed in the later section.

Table 21. Pressure-temperature ratings of Alloy 800H at temperature range of 800 to 1400°F.

Design Pressure (MPa)													
Temperature (°F)	800	850	900	950	1000	1050	1100	1150	1200	1250	1300	1350	1400
Temperature (°C)	426.7	454.4	482.2	510.0	537.8	565.6	593.3	621.1	648.9	676.7	704.4	732.2	760.0
NPS 2 ft SCH 160	21.80	21.40	21.01	20.62	20.42	20.03	19.64	18.26	14.53	11.58	9.23	7.46	5.89
NPS 1.5 ft SCH 160	21.67	21.28	20.89	20.50	20.30	19.91	19.52	18.16	14.45	11.52	9.18	7.42	5.86
NPS 2.5 ft SCH 160	19.71	19.35	19.00	18.64	18.47	18.11	17.76	16.51	13.14	10.48	8.34	6.75	5.33

Table 22. Pressure-temperature ratings of SS 316 at temperature range of 100 to 900°F.

Design Pressure (MPa)												
Temperature (°F)	100	200	300	400	500	600	650	700	750	800	850	900
Temperature (°C)	37.8	93.3	148.9	204.4	260.0	315.6	343.3	371.1	398.9	426.7	454.4	482.2
NPS 2 ft SCH 80	22.07	22.07	22.07	21.30	19.86	18.76	18.32	17.99	17.76	17.54	17.32	17.21
NPS 2 ft SCH 40	13.85	13.85	13.85	13.36	12.46	11.77	11.49	11.28	11.15	11.01	10.87	10.80
NPS 1 ft SCH 80	32.01	32.01	32.01	30.89	28.81	27.21	26.57	26.09	25.77	25.45	25.13	24.97
NPS 1/2 ft SCH 80	39.37	39.37	39.37	37.99	35.43	33.46	32.68	32.09	31.69	31.30	30.90	30.71
NPS 1/2 ft SCH 40	24.49	24.49	24.49	23.63	22.04	20.81	20.32	19.96	19.71	19.47	19.22	19.10

Table 23. Parameters for pipes in the pressure-temperature ratings.

Material	Nominal Pipe Size	Outer Diameter/ D (mm)	Nominal Wall Thickness/ t_m (mm)	Pressure Design Thickness/ t (mm)	Inside Diameter/ d (mm)	Velocity of Fluid/ V (m/s)
800H	2 ft SCH 160	60.33	8.712	7.712	42.906	6.49
800H	1.5 ft SCH160	48.26	7.137	6.137	33.986	10.35
800H	2.5 ft SCH160	73.03	9.525	8.525	53.98	4.10
SS 316	2 ft SCH 80	60.33	5.537	4.537	49.256	0.20
SS 316	2 ft SCH 40	60.33	3.912	2.912	52.506	0.17
SS 316	1 ft SCH 80	33.4	4.547	3.547	24.306	0.81
SS 316	1/2 ft SCH 80	21.34	3.734	2.734	13.872	2.49
SS 316	1/2 ft SCH 40	21.34	2.769	1.769	15.802	1.92

6.2 Preliminary Pipe Sizing

Generally, for the selection of appropriate pipe size, there are several factors needs to be estimated. As is known, smaller pipes require less purchase cost, while require larger pumping power. On the contrary, larger pipes require more purchase cost with less pumping power required. Especially when fluids have to be pumped through pipe (i.e., no natural circulation considered) the pipe size should be selected to give the least annual operating cost. A rule of thumb in chemical engineering gives guidelines to estimate pipe size based on experience on pipe velocities and allowable pressure drop, as shown in the Table 24 below [32].

Table 24. Typical pipe velocities and allowable pressure drops.

	Velocity (m/s)	ΔP (kPa/m)
Liquids, pumped (not viscous)	1-3	0.5
Liquids, gravity	n/a	0.05
Gases and vapors	15-30	0.02 per cent of line pressure
High-pressure steam, >8 bar	30-60	n/a

Simpson (1968) also gives value for the optimum velocity in terms of fluid density. The maximum velocity should be kept below that at which erosion is likely to occur. The values are listed in Table 25 below [32].

Table 25. Optimum velocities recommended in terms of fluid density.

Fluid Density (kg/m3)	Velocity (m/s)
1600	2.4
800	3.0
160	4.9
16	9.4
0.16	18.0
0.016	34.0

These suggested optimum velocity values are probably based on the purchase and cost information at that time. Studies have shown that the optimum velocity has shifted downward over past at least 40 years. Then it is reasonable to believe that the fluid velocity corresponding to the selected pipe size should be less that the value in Table 22.

In addition, in the review of literature, as to helium flow, 25 m/s velocity is recommended as a reference for economic velocity [Error! Reference source not found.]. In this report this value has been further xamined to estimate economic pipe diameter for helium loop in the INL facility using Genereaux equation (1937). Also it can be used to examine the steam line fluid velocity and pipe size selection.

In general, total pipe cost consists of two parts: capital cost and operational cost. The capital cost tends to increase with increasing pipe diameter due to increasing pipe material content. In contrast, the operational cost decreases with increasing pipe diameter because larger pipe size may generate less friction in the fluid flow thus pumping power is less required. Figure 19 shows the relationship of these two constitutes of total pipe cost. This can be expressed by Equation (54). The purpose to find economic pipe size is to differentiate the total cost to make it equal to zero, as shown in Equation (55**Error! eference source not found.**) [32][33].

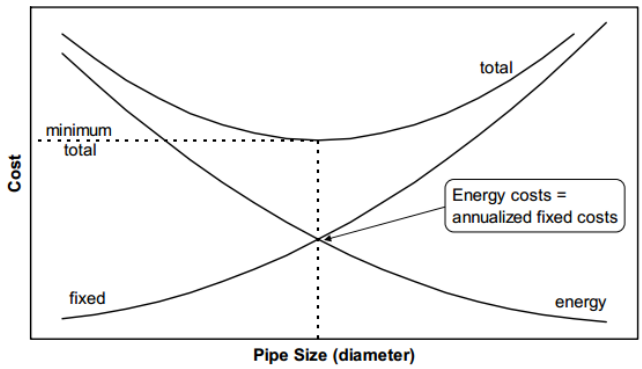

Figure 19. Relationship between capital cost and operational cost versus pipe diameter.

$$C = C_c + C_e \tag{54}$$

$$\frac{\mathrm{d}C}{\mathrm{d}d} = \frac{\mathrm{d}C_c}{\mathrm{d}d} + \frac{\mathrm{d}C_e}{\mathrm{d}d} = 0, \frac{\mathrm{d}C_c}{\mathrm{d}d} = -\frac{\mathrm{d}C_e}{\mathrm{d}d} \tag{55}$$

Genereaux has given the expression of these two parts of cost. For the pipe purchase cost, a model is generated as shown in Equation (56) [32][33]:

$$C_c = Bd^x(1+F)(a+b)L \tag{56}$$

In the equation, B and x are parameters strongly dependent on the pipe material and schedule; F is the factor that includes the cost of valves, fittings, and erection for a typical run of the pipe; a and b are capital charge and maintenance costs in terms of percentage; and L is the length of pipe. For the pumping power cost, a model is expressed as Equation (57) [32][33]:

$$C_e = AC_{en}P \tag{57}$$

where A is the facility attainment in terms of hours/year, C_{en} is the cost of power in units of \$/kWh, and P is the pumping power. For the pumping power, it is given by [32]:

Power = Volumetric flow rate × Pressure drop,

as is shown in Equation (58), where $\dot{m}$ is mass flow rate, Δp is pressure drop in L of pipe, ρ is the density of fluid, and E is the pump efficiency in units of percentage.

$$P = \frac{\dot{m}\Delta p}{\rho E} \tag{58}$$

Pressure drop consists of two parts: friction pressure drop Δp_{fr} and minor pressure drop losses Δp_{ml}. By introducing a ratio (J) of minor to friction pressure drop losses, the equation can be casted into Equation (59a). Combined with classic friction pressure drop calculation expression, the total pressure drop can be obtained from Equation (59b) [33].

$$\Delta p = \Delta p_{fr} + \Delta p_{ml} = \Delta p_{fr} + J\Delta p_{fr} = (1+J)\Delta p_{fr} \tag{59a}$$

$$\Delta p = (1+J)\xi\frac{L}{d}\frac{\rho u^2}{2} = (1+J)\frac{8}{\pi^2}\xi\frac{L\dot{m}^2}{\rho d^5} \tag{59b}$$

With fanning factor ξ formula used in Genereaux equation shown in Equation (60) [33]:

$$\xi = K\,\mathrm{Re}^{-k} \tag{60}$$

we can therefore calculate the optimum pipe diameter, with the final expression shown in Equation (61).

$$d^{5-k+x} = \frac{8(5-k)K}{4^k \pi^{2-k}} \frac{(1+J)AC_{en}}{BxE(1+F)(a+b)} \mu^k \frac{\dot{m}^{3-k}}{\rho^2} \tag{61}$$

For helium loop pipe size optimum selection, unfortunately this expression cannot be easily calculated due to the lack of information of individual parameters. According to the updated rules for pipe sizing [34], no data is available for nickel-based pipe material (for instance, 800H), and other parameters, such as A, need discussion (here it is assumed that the facility may operate with 30% time in a year). In addition, this expression is based on the assumption of smooth pipe flow, with fanning factor calculated in the form of Equation (60). In the calculation, Equation (62) has been used in the later analysis [33].

$$\xi = 0.04\,\mathrm{Re}^{-0.16} \tag{62}$$

It is necessary to reexamine its validation, and the correlation might not be applicable to helium flow with high Reynolds number. In reality, this estimation is too complicated to give useful guide towards pipe size selection unless relative accurate estimation of the parameters is available. However, based on parameters for stainless steel (shown in Table 26) and fanning factor correlation given by Equation (62), we can calculate the pipe diameter as a reference for the selection.

The results show that reference pipe inside diameter for helium flow loop is around 37.3 mm, and corresponding flow velocity 7.59 m/s. This value of velocity is far below what is recommended from literatures, indicating deviation from the values of terms used in the Genereaux equation calculation, but somehow matches the pressure rating results, which indicates that 1.5 ft SCH 160 (d=33.986 mm) and 2 ft SCH 160 (d = 42.906 mm) are suitable for current design conditions. Further investigation shows that with helium flow velocity being 25 m/s, the inner diameter of pipe must not be less than 21.87 mm, considering the highest temperature condition in the helium loop. It is obvious that both pipe sizes mentioned before satisfy the Genereaux results, and the inside diameter of both is greater than the limiting diameter requirement. We can make a preliminary conclusion that the pipe sizing for helium loop should be either NPS 1.5 ft SCH 160 or 2 ft SCH 160.

Table 26. Values used in the Genereaux equation.

Terms	Values	Description
x	0.924	Stainless Steel 2008
B	30.7	Stainless Steel 2008
E	0.5	Universal Assumption
J	0.5	Assumption
$a+b$	0.2	Universal Assumption
C_{en}	0.07$/kWh	North America 2008
A	2628hrs (=30%×365×24hrs)	Assumption
F	7.4	Stainless Steel 2008
μ_{helium}	4.2017×10^{-4} Pa-sec	Helium Flow at 600°C
ρ_{helium}	3.8243 kg/m^3	Helium Flow at 600°C
$\dot{m}_{helium}$	0.0316 kg/sec	Nominal Helium Flow Rate
μ_{steam}	2.2944×10^{-5} Pa-sec	Steam at 350°C
ρ_{steam}	87.11 kg/m^3	Steam at 350°C
$\dot{m}_{steam}$	0.0327 kg/sec	Nominal Steam Flow Rate

Similarly, the calculating results from Genereaux equation also show that for steam line pipe the reference pipe inside diameter is around 13.1 mm, with corresponding fluid velocity about 2.77 m/s. Combined with the pressure rating analysis, it is seemingly convincing that 1/2 ft SCH 80 pipe will possibly become the optimum pipe size for steam line in terms of steam flow at 350°C. Although there are some uncertain factors such as *A* (facility attainment factor) and fanning factor correlation selection, the variation would not generate large deviation from the current result. Therefore, it is recommended to select NPS 1/2 ft SCH 80 pipe as steam line pipe geometry.

This preliminary recommendation on pipe size needs further research and more reliable data to determine the detail of pipe geometry.

7. CHEMISTRY CONTROL: PART I

7.1 General

The experience of large scale molten fluoride salts production preparation and chemistry control is primarily based on ORNL Molten Salt Reactor Experiment (MSRE) program. Therefore, this chapter has necessarily summarized the studies and experience obtained in MSRE to provide an overview in (1) salts mixture production and preparation, (2) chemistry control, (3) systems and equipment, (4) process operating conditions.

In the MSRE program, molten fluoride salts BeF_2-LiF with uranium fuel was used as primary fuel salts. The same chemical composition of salts was applied to the secondary coolant salts and other flush salts. ZrF_4 was also used in the fuel-bearing salts for the purpose of prevention of fuel oxides precipitation. These starting raw materials were purchased from commercial resources except uranium tetra-fluoride. As to the procurement of lithium fluoride, isotopic purity of ^7Li was required only due to neutron-absorption cross-section consideration, which would not be required in the case of INL facility design. Zirconium tetra-fluoride free of hafnium (<50 ppm) was procured commercially.

The fluoride production method is generally independent of fluoride mixture composition provided that the liquidus temperature of salts can be reached by the process equipment. In the case of current design, only LiF and ZrF_4 will be combined. Therefore, the procedures of salts mixture production based on MSRE experience will be simplified. Because of the beryllium used in the MSRE, its toxicity required complex facilities and procedures to prevent hazardous conditions to personnel and to confine fluoride contaminants. Most of the working area was isolated. In our case, the handling of raw starting materials will not necessarily require such restriction. Generally, during the production process, materials (salts) were fed through the tube of vibratory conveyor and dropped into furnace assembly to meltdown. In the furnace vessel different raw materials were molten down and mixed, which might require 4 to 6 hr. At the same time, gas purge took away volatilized water vapor and carbon as well as metallic reducing agents were added to reduce sulfates and structural-metal fluorides. After the pretreatment, salts mixture was charged to processing units by decantation, which was to separate any insoluble materials.

The processing units consisted of two primary salt containers, a salt treatment vessel and salt storage vessel (salt receiver). They have been essentially connected by a small diameter tube as either a gas treatment line or salt transfer line. The gas for chemical treatment would flow through this connecting line to sparge fluoride salts in the treatment vessel. Additionally, salts would be discharged to the salt receiver at the completion of treatment process. There were several auxiliary systems affiliated to the processing units served as gas treatment equipment. As discussed later, HF and H_2 gas was used to remove oxide, sulfur and structural-material impurities. The chemical process would be completed in this system to ensure the quality of salts. Finally, it was documented that batch-sized containers were used to accomplish storage and transportation of prepared bulk mixture salts in terms of economic consideration.

It had been recognized that impurities in mixture salts play an important role in corrosion to structural materials. In the initial stage of corrosion to the structural materials, the oxidizing contaminants in the

molten salts, usually moisture or other impurities, becomes predominating in the corrosion process. Some of the oxidizing impurities result from the absorbed moisture during the production process of salt mixture. Thus H_2O is one of the most deleterious contaminants in fluoride salts as stated in the literature with the reaction with alkali fluorides (63) [6]:

$$\begin{aligned} MF(l) + H_2O(g) &\rightarrow MOH(l) + HF(g) \\ 2MF(l) + H_2O(g) &\rightarrow M_2O(l) + 2HF(g) \end{aligned} \tag{63}$$

Other sources of impurities are possibly from starting materials, such as iron. In addition, some of the metal fluoride impurities (also known as structural-material impurities) originate from the initial corrosion of fluoride salts to structural materials, which in turn accelerate later corrosions driven by those impurities. In general, these impurities can lead to chromium depletion from the surface of the structural material in contact with fluoride salts as rapid corrosion attack to facility structures. It is stated that when these oxides or impurities are exhausted, this type of corrosion will cease. Thus eliminating impurities continuously, or routine chemistry control during operation, is of great importance. In this section removal of oxide, sulfur, and structural-metal impurities will be discussed.

The treatment used in the program of ORNL MSRE to remove oxides was to sparge the molten fluoride melt with anhydrous hydrogen fluoride. They react directly with oxides by the reaction (64) [35,36]:

$$O^{2-} + 2HF \rightleftharpoons 2F^- + H_2O \tag{64}$$

Oxides are removed continuously from the process as water vapor. The treatment with HF is recommended to be continued beyond reaction completion to ensure capability of removing inadvertent contamination [35].

It is noteworthy that HF imposes great corrosive threats to structural materials such as treatment vessel. A solution was applied to avoid corrosiveness, which was to utilize alternate gas treatment with HF and H_2. However, this treatment, which could to some extend prevent serious corrosion, had some drawbacks. Though in the gas phase of treatment vessel, for example, an impervious layer of structural-material fluorides will be formed during treatment by the reaction (65) [35][36], in the liquid phase layers formed on the surfaces contacting molten fluoride salts may be renewed by dissolution of the layers. The alternating oxidation and reduction of structural-material during alternate gas treatment may eventually cause failure of vessel walls.

$$M^0 + 2HF \rightleftharpoons MF_2 + H_2 \tag{65}$$

Another solution was to use HF and H2 simultaneously, which had been tested in the Engineering Test Loop Facility in the MSRE. It was stated that this gas treatment was effective typically at HF concentration of 1/10 mole fraction admixed with H_2 [8]. It also prohibited the corrosiveness of HF-H_2O effluent gas mixture. Tests indicated that minor corrosions at the Inconel dip tube used for sparging the fluoride melt with HF-H_2 occurred [35].

Similarly, gas treatment with HF was used to remove sulfur in the MSRE. Sulfur is usually present in the form of sulfate, which needs to be first reduced to sulfide ion and then be volatilized as H_2S by reaction with HF. Alternate gas treatment with HF-H_2 was reasonably effective, but increased treatment times because of discontinuity of sulfide removal that affects quality control. Simultaneous gas treatment could continuously remove sulfate but removal rate is relatively low. Another concern is the need of rapid effective reduction of sulfate in the process because at high temperatures the products of thermal decomposition of sulfate may corrode salt container made of nickel or copper. Additional metallic reducing agents was used such as beryllium [35].

Removal of structural-metal impurities can ensure no initial rapid chromium depletion happen. Typically, the concentration of chromium at the surface adherent protective layer decreases due to the oxidation of chromium with impurities, for example, in the reaction with iron fluoride (66):

$$Cr + FeF_2 \rightleftharpoons CrF_2 + Fe \quad (66)$$

This results in the chromium diffusion from subsurface of the alloys and the formation of voids at subsurface area. This corrosion mechanism is termed as "chromium depletion." Additionally, the metal products of the chromium fluorination may be dissolved in the fluoride salts again and then continue corroding structural materials. Generally, the chromium depletion can be induced by HF, NiF_2, FeF_2, and FeF_3, etc. It has been recognized that the chemistry control of these impurities can greatly reduce the initial rapid corrosion as chromium depletion.

In the MSRE, hydrogen treatment as a final gas sparge treatment was applied to remove these impurities. This solution is based on the reaction (65) as hydrogen reduces metal fluoride. This treatment, similarly, was later replaced by HF-H_2 mixture gas. It was mentioned in the documents that nickel fluoride was the readiest one to remove, followed by iron fluoride, and that chromium fluoride was the most difficult one. But the concentration of chromium was acceptable at most of time so that no development of chromium impurities removal was necessary. It was stated that the higher hydrogen flow rate leads to better removal of impurities. However, too high hydrogen flow rates (10 liters/min) [35] caused frequent entrainment of salt in the gas effluent lines.

An alternative method to remove metal impurities was to add beryllium or zirconium when an exceedingly high concentration of structural-metal fluoride was present and it was necessary to reclaim the metal loss from corrosion [35].

7.2 System Description and Process Operating Condition

Typically in the MSRE salt preparation facility, fused fluoride mixtures were produced in two batch processing units as mentioned before. Prior to the production of salt mixtures, each batch unit was individually loaded with starting material from a transfer hopper. A normal batch meltdown might take 4 to 6 hours and cooling period might take about 48 hours. Because of the repeated procedures and identical chemical composition requirement, it was feasible to use single furnace equipment to accomplish multiple batch productions. The relocation of starting raw materials was adjacent to meltdown furnace so that the materials handling was convenient.

The meltdown furnace assembly mainly consisted of a vessel constructed of 6-ft of IPS 12-in. SCH 40 SS 304L pipe lined with 1/8-in. nickel sheet, and a 50-kVA furnace of commercial design surrounding the vessel. After the production, salt mixtures were then transferred to processing units. These units primarily consisted of two salt containers, of which the larger one was the salt treatment vessel, constructed of 6-ft length of 12-in. IPS 304L stainless steel pipe lined with 1/8-in. Grade A nickel sheet to accommodate bulk salt around 2 ft^3 in the molten state, and the smaller one was the salt receiver constructed of Grade A nickel, 12 in. in diameter and about 3 ft. in length to store salts after salt purification had been finished. Both vessels were surrounded by furnace assembly, with 50 kVA and 23 kVA heating capability, respectively. They were connected by a small-diameter tube, which dipped in the treatment vessel, primarily serving as a connecting line through which process gas could pass and salt charge could flow. This system is shown in the Figure 20.

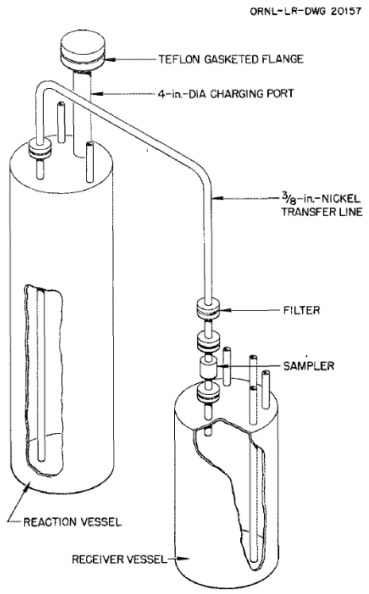

Figure 20. Fluoride production facility – salt treatment and receiver vessel [35].

The processing units were connected with process control systems as shown in Figure 21. The gas line system provides either for alternate use of hydrogen and helium, etc., or for mixing anhydrous hydrogen fluoride with hydrogen. The flow rates of hydrogen and helium were controlled by flow meters, while the concentration of hydrogen fluoride was determined by direct titration of a side stream with standard caustic solution. The process control was primarily based on the results of off-gas analyses. The concentration of hydrogen fluoride, using the same method mentioned above, was analyzed to check the material balance such as oxide content remained in the salts. Additionally, the cold trap in the system was used to collect water vapor, which was indicative of the oxide removal rate. The exhaust hydrogen fluoride was absorbed by sodium fluoride pellets right after the cold trap device. Finally, waste gases were bubbled through a seal pot filled with fluorocarbon oil and then exhausted to the ambient environment.

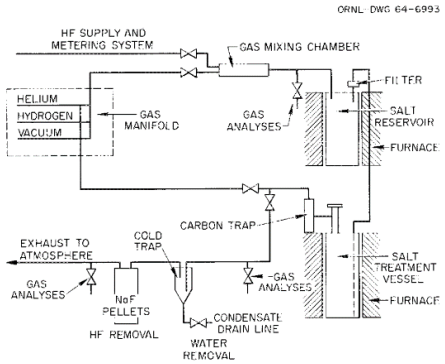

Figure 21. Fluoride production facility – simplified schematic process diagram [20].

The operating conditions during the process of fluoride mixtures were determined through prior production practices and existing equipment. They were also affected by several factors. With regard to temperature setting for HF-H_2 treatment, a lower temperature was favored according to the oxide removal rate. As to the concentration of HF in the mixing gas, we need to consider the equilibrium condition of both reactions (Equation 64) and (Equation 65). Since the vessel was usually lined with nickel sheet, the reaction (Equation 65) can be presented by reaction (Equation 67) [35]:

$$Ni^0 + 2HF \Leftrightarrow NiF_2 + H_2 \quad (67)$$

From the experience of MSRE salt processing, 600°C was chosen as oxide removal process temperature. It is stated that based on the set requirement that NiF_2 is maintained at 25 ppm, at 600°C the hydrogen fluoride concentration in hydrogen would be about 38% in volume whereas at 500°C decrease to 23% [35]. Basically, higher temperature could yield less nickel corrosion from hydrogen fluoride. Studies had shown that low HF concentration was sufficient for effective oxide removal. In the MSRE the concentration was set 10% in hydrogen at 1 atm pressure. The treatment of HF would be eased when water evolution rate reached set bottom value of 2 g/hr in the analysis of off-gas content due to the sensitivity of analytical system. As calculated from equilibrium data, it corresponded to oxide content in the melt varying from 0.44 ppm at 600°C to 0.02 ppm at 500°C [35]. It was mentioned that higher concentration of HF was not suggested primarily because of the introduction of complicated systems. Higher concentration of HF used in the gas treatment might result in no permission of direct discard of hydrogen mixing effluent to the atmosphere, and also require increased operator attention. No development effort was thus continued.

As to sulfur removal, which was based on the same HF-H_2 gas treatment method, the effective removal rate was difficult to achieve. H_2S evolution rate was analyzed in the off-gases, and material balance calculation always indicated mismatch of sulfur removal with what was anticipated. It was explained that this might result from the deposition of nickel sulfide. As discussed in the last section, reducing metallic agents such as beryllium could be used for rapid reduction of sulfate. Accordingly, the addition of these agents was helpful to complete sulfur removal assisting the gas treatment, as it was. At the same time, when an addition of reducing metals failed to result in an increase in the H_2S evolution rate, which corresponded to the remaining content of sulfur in the melt, it was considered that the removal had been effective. This had been confirmed with less than 5 ppm of sulfur in the finished batch.

As to structural-materials impurities removal, it was generally believed to be accomplished by a final gas (i.e., hydrogen) treatment to the salt mixtures at the treatment vessel. However, at the pretreatment stage when raw salts were meltdown at the furnace, reducing metallic agents such as beryllium were added to reduce the content of metal fluorides. Though this pretreatment method was constricted by liquid-solid separation process when salts were charged to treatment vessel, it had been studied that iron concentration had been greatly reduced to 200 ppm. The separation technology difficulties resulted in decantation instead of filtration at the transfer of salts from meltdown furnace to the treatment vessel.

At the final purification stage, beryllium and zirconium were demonstrated to be effective. However, it was limited by certain process conditions. It was believed that the surface coating of these active metals lead to nonstoichiometric analysis of impurities. Furthermore, the fact that some of these metals were suspended in the melt reduced their effectiveness. The process control to ensure satisfactory reduction could increase time for chemical analysis and offset the time saved by rapid reduction. Therefore, the addition of large excesses of active metals was not advised.

The removal of structural-materials impurities was primarily dependent on hydrogen treatment. The operating temperature was raised to 700°C with increased reduction rate. Hydrogen fluoride was also present in the hydrogen, serving as an indicator of iron fluoride remained in the melt based on the reaction (65). It was assumed that it was a steady-state process, so that the concentration of hydrogen fluoride could be associated with the one of iron fluoride.

8. CHEMISTRY CONTROL: PART II

8.1 General

In the previous chapter, the past experience in using HF combined with hydrogen (H_2) has been summarized. This method has been intensively used in MSRE program. Recently, more attention has been paid to another candidate, nitrogen trifluoride (NF_3), which is expected to remove oxide and

hydroxide containments from the molten salt coolants without many chemical hazards. Its potential as a removing agent has been evaluated by the Pacific Northwest Laboratory [37], and related removal techniques have been developed at the UW-Madison [38].

Most of the research has been carried out to compare NF_3 and HF/H_2 in terms of industrial use, chemical and physical properties, chemical and reactivity hazards, chemical viability, structural materials and systems requirement, release management and financial consideration, etc. The introduction of NF_3 will be unfolded in these aspects.

Generally, NF_3 displays mild toxicity at room temperature. In contrast, HF is highly toxic and corrosive at room temperature. With respect to chemical viability, the thermodynamic calculation in free energies of the reaction of NF_3 with postulated contaminants shows that it is a strong fluorinating agent in a wide range of operating temperatures. In contrast, HF reactions have been calculated to be less effective in removing contaminants when exposed to high temperature (300°C and above). However, it was still proved successful when applied in MSRE program. Cautions seem to be necessary when using NF_3 in a plant because of the potential adiabatic compression in the systems that may result in thermal decomposition. The material requirements for both fluorinating gas agents are similar. Additionally, NF_3 has been identified as one of potential contributor to global warming, which requires certain release management. Finally, the comparison of both gases' price has been provided to give a basic financial perspective on their potential application in INL project.

8.2 Comparison of the Applications of NF_3 and HF

As is commonly known, hydrogen fluoride is a highly toxic and corrosive gas that harms people's health if they are exposed. Furthermore, it is highly reactive and corrosive to metals, and it can produce heat and toxic fumes in those reactions. Therefore, necessary care should be taken to prevent significant health and safety effects. However, nitrogen trifluoride is mildly toxic, non-corrosive, and non-flammable. It is also relatively inert at room temperature and pressure, but displays reactivity hazards when sufficient energy is provided, which may result from high-temperature operation conditions, inappropriate mechanical designs that cause adiabatic compression or shocking, flow friction within systems and localized hot spots, etc. The mechanism of its increasing reactivity is that the thermal decomposition of NF_3 produces highly reactive species that will react with most materials, which may cause more heat and in turn induce more thermal decomposition. This self-propagating reaction can be effectively managed with several precautions, which includes:

1. Operating temperature should be as low as possible. At temperatures above 300°C, the decomposition of NF3 will dramatically increase with increasing temperatures.
2. NF3 flow pressure and velocity should be strictly managed. This is primarily because of the flow friction hazards at high pressure and velocity scenarios. The recommendation of flow pressure and velocity control are described as follows:
    a. For pipeline pressure above 15 bar (1.5 MPa), the maximum NF_3 velocity should be controlled such that the product of the velocity and pressure in the pipeline does not exceed 450 bar m/s.
    b. For pipeline pressure below 15 bar (1.5 MPa), the velocity should be controlled less than 30 m/s.
3. Local mechanical shocks and adiabatic compression should be prevented. Sudden pressure change may induce rapid temperature increase, and if the heat generated cannot be dissipated quickly, the thermal decomposition may possibly happen. This requires the systems design to eliminate the use of ball valves, sharp pipe bends, etc.
4. Materials of construction should be selected to be compatible and clean, and have high thermal conductivities. Clean materials are concerned with the reduction of potential flow friction. Also, materials with high-thermal conductivities will effectively transfer the heat generated inadvertently in the local spots of systems away to prevent thermal decomposition of NF_3. In the literature, it is

recommended to use stainless steel, carbon steel, and nickel alloys for low and moderate pressure (up to 10 MPa); and nickel, nickel alloys, and copper for high pressure (greater than 10 MPa). Critical components are suggested to be constructed of copper and its alloys, nickel, and Monel®.

In the previous chapter, HF/H_2 as a fluoride coolant purification agent has been introduced. The major disadvantage found in the first method with only anhydrous HF was the corrosiveness of HF to the vessel metal. The second method with HF/H_2 gas treatment, which also eventually became the baseline gas treatment method in MSRE program, limited the level of HF that could be present in the feed gas stream considering the potential of corrosiveness. With respect to NF_3 as fluoride coolant purification agent, it is evaluated to be effective based on its performance in purifying fluoride glasses in industrial application. Additionally, studies on HF and NF_3's chemical viability have been carried out to further evaluate the potential replacement of NF_3 in removing contaminants from molten salts.

The rationale to perform chemical viability studies is to calculate the thermodynamics of the reaction of NF_3 and HF with potential contaminants. The general approach is to input the thermodynamic properties of oxide or hydroxide contaminants, mixed-fluoride salts and HF and NF_3, of which the data are provided by HSC Chemistry database. The thermodynamic properties include enthalpy of formation (ΔH_f), entropy of formation (ΔS_f), and free energy of formation (ΔG_f). The method of the calculation is quite straightforward. The reaction enthalpy is calculated by subtracting the sum of the heat of the reactants from the one of the products. For example, for the reaction shown below [37]:

$$X + Y \Leftrightarrow X_2Y \tag{68}$$

the reaction enthalpy change ΔH_{rx} would be:

$$\Delta H_{rx} = \left(1 \times \Delta H_{f(XY)}\right) - \left(2 \times \Delta H_{f(X)}\right) - \left(1 \times \Delta H_{f(Y)}\right). \tag{69}$$

Other calculations are somehow likewise. A reaction is thermodynamically favorable if the corresponding ΔG_f is negative. Typically, that ΔH_f is negative also indicates that a reaction is favorable.

One of the calculation results will be briefly shown in this chapter. $KF\text{-}ZrF_4$ has been identified to be the fluoride molten salt candidate used in the INL loop design. The thermodynamic calculations of the fluorination of potential zirconium oxide are presented as shown in Table 27.

Table 27. Calculated thermodynamic values for fluorination of ZrO_2 by NF_3 and HF [37].

T,°C	$1.5ZrO_2 + 2NF_{3(g)} = 1.5ZrF_4 + N_{2(g)} + 1.5O_{2(g)}$			$ZrO_2 + 4HF_{(g)} = ZrF_4 + 2H_2O_{(g)}$		
	ΔH	ΔS	ΔG	ΔH	ΔS	ΔG
	kJ/mol F	kJ/mol F	kJ/mol F	kJ/mol F	kJ/mol F	kJ/mol F
100	-158.5	11.0	-162.6	-50.4	-65.9	-25.8
200	-158.2	11.7	-163.7	-50.4	-65.9	-19.2
300	-157.9	12.1	-164.9	-50.3	-65.7	-12.6
400	-157.7	12.5	-166.1	-50.0	-65.3	-6.1
500	-157.2	12.8	-167.4	-49.7	-64.8	0.4
600	-157.2	13.2	-168.7	-49.1	-64.1	6.9
700	-156.8	13.6	-170.0	-48.5	-63.5	13.3
800	-156.4	14.0	-171.4	-47.8	-62.0	25.8
900	-155.9	14.4	-172.8	-46.9	-62.0	25.8
1000	-140.2	27.7	-175.4	-30.8	-48.4	30.8

Both NF_3 and HF have shown capabilities to effectively remove ZrO_2 because the ΔH remains negative in the range of temperatures up to 1000°C. However, it is observed that ΔG for HF reactions increases beyond zero with increasing temperatures, which implies that the reaction at high temperature requires excess of HF and/or removal of H_2O product. In contrast, for NF_3 reactions, ΔG values are still negative, which proves NF_3 to be a stronger fluorinating agent than HF, at least in removing ZrO_2 impurities. More details can be found in the literature. In summary, it can be concluded that with the fact that most of the NF_3 reactions with contaminants present in molten salts will be more favorable than those corresponding reactions of HF, NF_3 will also successfully fluorinate the impurities and perform duties that have been done by HF treatment in MSRE program. However, this type of calculation can only serve as indicator. More intensive experimental studies need to be carried out in the future.

Table 28 has summarized the comparison of two different fluorination methods.

Table 28. Summary of the comparison of NF_3 and HF in applications to molten fluoride salts purification.

Comparison	NF_3	HF
Chemical and reactivity hazards	Mildly toxic	Highly toxic
	Non-corrosive	Corrosive to structural materials
	Non-reactive at room temperature; reactive with metals or alloys at high temperature	Reactive with metals to release toxic fumes or explosive hydrogen
Chemical viability	Effective at removing oxidizing contaminants; stronger fluorinating agents than HF	Applied in MSRE program; Proved successful in fluorination
Structural materials and systems requirement	Pure nickel metal or nickel-based alloys	Pure nickel metal or nickel-based alloys
	Reactive at temperatures above 300°C due to thermal decomposition into reactive species	
Release management	Global warming contributor	No significant environment effect
Financial consideration	\$10.05/mol NF_3 \$64.32/lb	\$1.25/mol HF \$28.30/lb
Comprehensive	Viable and effective purification agents	Experience in MSRE program
	Slightly toxic and non-corrosive	Highly toxic and corrosive
	Careful engineered systems required	Mixture with hydrogen required; potentially explosive
	Released strictly controlled	Protection from toxicity

8.3 Current Relevant System Design for NF_3 Application

One reaction vessel design developed in UW-Madison was used as a fluoride salt purifier that is based on ORNL's batch purifier. The schematic of the reaction vessel has been presented in Figure 22. It consists of a nickel reaction vessel surrounded by heaters and insulation material and outmost a SS 304 pipe serving as a main structural support. The principle components in this purification system include salt and gas transport line system, heater assembly, and structural support.

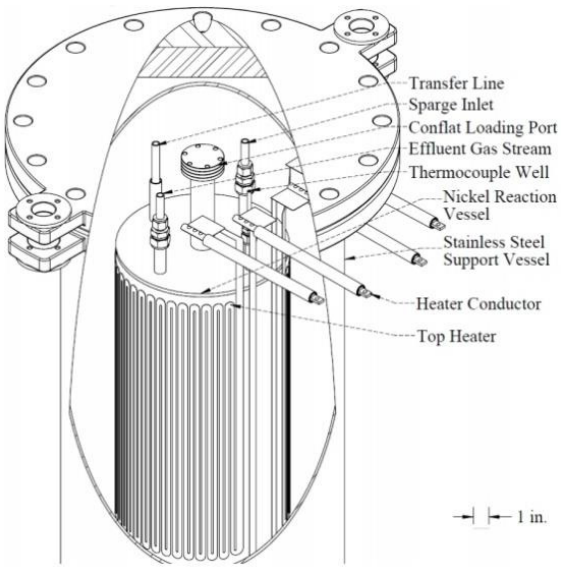

Figure 22. The UW-M fluoride salt purifier design schematic [38].

From the schematic it is observed that there are several ports protruding from the top of reaction chamber where fluoride salts are treated. The largest port, made of nickel 200, is used for transport raw salts and solid purification reduction agents into reaction chamber, which is 1.5 in. in diameter and 6 in. high from the top of lid. Two of the openings that are attached to 3 in. tall, 3/4 in. outer diameter, nickel 200 nipples are used for sparge tube and effluent gas stream. These sparge tubes extend to the very bottom of the reaction vessel for the similar purpose in the ORNL's design. Another .75 in. nipple is welded to the transfer line. The last opening is attached to a 3 in. tall, .5 in. outer diameter nickel nipple that is connected to a sealed thermocouple well stretching downwards to the bottom of the reaction vessel.

The heat assembly wraps around the nickel reaction vessel with two heating zones: top and bottom. The top heating zone is visible in the schematic figure. Each zone is cut from a 0.020-in.-thick Inconel 625 sheet, with 79.5-in.-wide strips on the 22-in.-tall top heating zone, and 85.5-in.-wide strips on the 11-in.-tall bottom heating zone. The top and bottom heaters' resistance are 18 Ω and 12 Ω, respectively. The heaters can generate overall 8 kW of power. The entire heater systems reach out the top and terminate at a large plate visible in the figure that is connected to four separate .5-in. copper conductors. These copper conductors are placed in SS 304 tube.

Wrapped around the heater assembly is a sheet of mica followed by 3.5-in.-thick of microtherm powder insulation. Outside of insulation is a 48 in. tall, 18 in. outer diameter, SCH 5 SS 304 pipe as the main structural component. It is sealed by a 1.5-in. thick SS 32 lid at the bottom and a class 150 flange assembly on the top. The bottom is also welded flush with the pipe.

9. COMPONENTS AND INSTRUMENTS

9.1 Flowmeters

In the OSU HTHF, three Venturi meters are used for measuring the working fluid's flow rate. These meters were constructed of SS 316 by Flow-Dyne Engineering. Each meter was calibrated by Flow Dynamics. Their operational Reynolds number fall in the range of around 12 to 360 × 10^3 [19]. This type of flow meters may require higher initial cost, but become competitive with other kinds of flow meters based on comprehensive ownership cost, application in extreme temperature and pressure conditions, etc. As one of the traditional pressure differential flow meters invented in 1895, Venturi meters have a long

operational history to ensure its accuracy. The principles for Venturi meters operation are primarily based on Bernoulli equation as given below:

$$p_1 + \frac{1}{2}\rho_1 V_1^2 + \rho_1 g h_1 = p_2 + \frac{1}{2}\rho_2 V_2^2 + \rho_2 g h_2 \tag{70}$$

where p, ρ, V, g and h are the static pressure, density, mean velocity, gravitational acceleration and height, respectively. Subscripts 1 and 2 denote the upstream and downstream conditions, respectively. Typically, a Venturi meter consists of a throat section of pipe, of which the inner diameter is smaller than pipe diameter in order to accelerate the fluid flow to generate static pressure differential between the upstream and throat location. The pressure differential Δp ($=p_1-p_2$) developed by the flow element is measured, and the volumetric flow rate Q or the mass flow rate W can all be calculated using the following generalized formulas:

$$\begin{aligned} Q &= KA\left(\frac{\Delta p}{\rho}\right)^{0.5}, \\ W &= KA\left(\rho \Delta p\right)^{0.5} \end{aligned} \tag{71}$$

where K and A are discharge coefficient of the Venturi meter and cross-sectional area of the pipe's opening. For an ideal gas application assuming incompressible pipe flow, Equation (72) [39] can be further modified to:

$$\begin{aligned} Q &= KA\left(\frac{p\Delta p}{RT}\right)^{0.5}, \\ W &= KA\left(\frac{RT\Delta p}{p}\right)^{0.5} \end{aligned} \tag{72}$$

where T is the upstream fluid temperature and R is the gas constant. The equations mentioned above only consider the ideal conditions. In reality, the real flow rates vary from the calculation, and can be accounted for using empirical equations to find an appropriate K value. However, for higher accuracy calibration is required.

Usually the Venturi type flow meters are used for flows of above 10^4 of Reynolds number, mainly to avoid any unstable characteristic rise in the coefficient of discharge in the transitional region. Another concern is its limited rangeability and associated accuracy of measurement. Rangeability, also known as turndown ratio, indicates the range of specific flow meter with acceptable accuracy in measurement. The limited rangeability value will impose constraints on its application for measuring a wide range of helium flow rates. In addition, Venturi meters do not measure the density directly, which means there is possibility that the deviation of the density value may result in errors in the mass flow rate measurement. Guidelines are given in the literature for reduction of density measurement errors, one of which suggests the ratio of the differential pressure (Δp) to the upstream pressure (p) not exceed 0.25 for compressible fluids [33]. In addition, the metering errors due to incorrect installation of primary element can be substantial. Thus, installation should be subject to official installation guides (for example, in OSU HTHF Venturi meters were installed at least 4 pipe diameters away in length after elbows and valves) [19].

For applications of molten salt flow rate measurements, literature review shows that several types of flow meters are acceptable for the current design condition. In the ORNL MSRE program, Venturi type meters were used for coolant salt flow rate measurement. It was measured by a high-temperature, NaK-filled differential pressure transducer [39]. Performance of this type meter was documented as

acceptable, and the service condition was similar to the current design. It can be considered as one of the candidates for molten salt flow rate measurements.

Ultrasonic flow meters have been considered to perform flow rate measurement without contacting salts directly. However, these meters are limited to a certain process temperature, usually below 500°F. The molten salt facility at the UW-Madison also encountered similar issue [Error! Reference source not found.]. Most f the available commercial ultrasonic flow meters fall in temperature ranges that are not suitable for a molten salt measurement application. Even when some of the products claimed operable at required high temperatures, the nominal flow rate was too small for these ultrasonic flow meters to accurately measure (50 g/min).

Based on the two criteria of ultrasonic flow meters on the market (i.e., high-temperature capability and suitable flow rate measurement range), we have found several products that are potentially possible to be used in the INL facility (listed in Table 29). As is known, in the current facility design the average velocity of KF-ZrF_4 approximates 0.1 m/s in the pipe with NPS 2 in. and SCH 40. UFM 530 HT from KROHNE, one of the candidates, claims to be capable of operating at up to 500°C and the measurement range covers 0.5 to 20 m/s [41]. Another product is Bundle Waveguide Technology System (BWT) from GE. It claims to be capable of withstanding up to 600°C operating temperature, with velocity ranges from 0.03 to 12 m/s for liquid [42]. The product to be used in OSU DRACS HTDF is FLUXUS ADM 7407 from FLEXIM, with operating temperature up to 400°C and measuring range from 0.01 to 25 m/s [43]. This information is obtained from technical datasheet, and further contact with manufacturer will be done in the next few weeks. We can draw a conclusion that it is still hard to find an appropriate product suitable for the INL facility. Some compromise in loop design will be necessary to utilize one of these candidates.

Table 29. Ultrasonic flowmeters candidate products' main parameters.

Products	Operating Temperature Limit (°C)	Measuring Velocity Range (m/s)
UFM 530 HT, KROHNE	500	0.5~20
BWT, GE	600	0.03~12
FLUXUS ADM 7407, FLEXIM	400	0.01~25

As to the issue of low-flow velocity, a design of changing pipe size at the section of flow rate measurement is proposed to address that challenge. Inspired by UW-Madison where a custom thermal flow meter was developed to measure flow rate, we can simply choose a section of a pipe and decrease the pipe size to obtain a higher flow velocity. To some degree, this can solve that issue without concern about flow meter applicable temperature.

Furthermore, there are other types of flow meters that have been mentioned in the literature. Turbine type flowmeters were once developed for the ANP program in ORNL, but proved to be failure after a short period of service due to the high-temperature physical properties of the turbine blade and bearing materials. It was still possible if improved material was available [40]. Magnetic flowmeters were once considered since they were extensively used at high-temperature liquid metals system to measure a variety of fluids. But in the application to molten salt, it became limited due to low electric conductivity. The penetration of electric lead may impose non-compatibility with molten salts. These considerations made this type of flow meters abandoned [40].

In summary, Venturi type meters and ultrasonic flowmeters are recommended for measurement of flow rate in the helium and molten salt loop, respectively. Further research is needed to address more comprehensive issues such as cost and installation.

9.2 Grayloc

The Grayloc Connector is a metal-to-metal seal connector with only three major components: metal seal ring, two hubs (one end is welded with a pipe), and clamp assembly, as shown in Figure 23. The metal seal ring is of self-energized bore seal, consisting of a rib and two lips. When a connector assembled, the lips of the metal seal ring deflect against the inner sealing surface of the hubs, while the rib is forced against the two hubs' surfaces. The lips are characterized by their self-energized seal when the hubs and the metal seal ring are clamped, and the ribs function as sealing, preventing leakage of fluid or gas in the piping. The clamp component is to fasten the entire connector, with no specific orientation of installation required, which may make the assembly flexible in the confined space and minimal clearance.

Figure 23. Assembly of Grayloc Connector.

According to the company's claim, the sealing integrity can be assured under various extreme circumstances. Grayloc Connectors can withstand greater tension loads than traditional flanges. Independent tests indicate good performance in bending loads. Applications in extreme service conditions are also listed, including high temperature up to 1700°F, fluid corrosion such as liquid sodium and wide range of pressure to withstand, from full vacuum to 60,000 psi (around 410 MPa) [44]. Due to the promising performances, Grayloc is announced to allow no maintenance under these severe situations.

Generally there are four advantages of using Grayloc over conventional ANSI or API ring joint flanges. To begin with, the size and weight is largely reduced. Secondly, a shorter length of weldneck makes it lighter and smaller. Additionally, due to the fact that the clamp can be rotated a full 360 degrees around the hub, the bolts' orientation is flexible, and the installation will not be restricted by limited space. Finally, as a result of freedom to rotate the clamp again, the bolts alignment may not limit the installation of other components, such as valves. Compared to traditional flanges, Grayloc Connectors are much lighter, smaller and flexible.

As to installation of Grayloc Connectors, time for make and break is reduced because of only 4 bolts required instead of 8 to 24 bolts on a conventional flange as well as smaller torque needed. The size is determined according to pipe size and schedule, leading to application to all piping of the same size regardless of pressure. These features save time and money for construction.

In the case of the application to fluoride molten salt systems, the cost of Grayloc connectors is increased mainly because of the larger size of hubs required to withstand high temperature than standard off-the-shelf products. From the quote OSU recently received, we can observe more than double priced overall quotes for the same 1-1/4 SCH 40 pipe size, which is around $330 for one hub, $127 for one seal ring and $397 for one set of clamp component.

9.2.1 Material Properties

Here list the thermal conductivity functions versus temperature of the materials used in the heat loss analysis. Both the function curves and data points are from manufacturer's datasheets and are shown in the figures below..

9.2.1.1 Alloy 600

The thermal conductivity of Alloy 600 can be given by:

$$k = 14.572 + 1.340 \times 10^{-2} T + 3.494 \times 10^{-6} T^2 \tag{73}$$

k is thermal conductivity in W/m-°C, and T is temperature in °C. Figure 24 plots both the tabulated data and function curve.

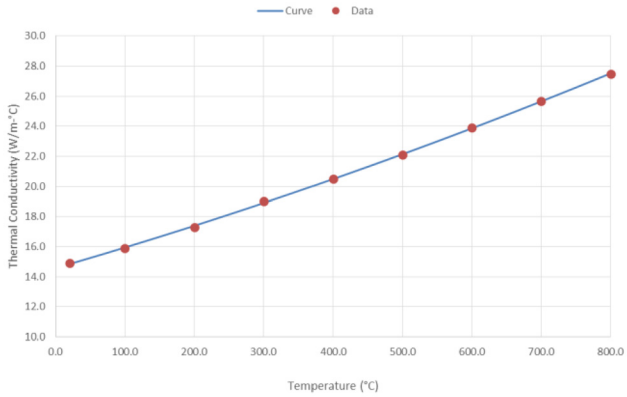

Figure 24. Thermal conductivity of Alloy 600 versus temperature.

9.2.1.2 Alloy 800H

The thermal conductivity of Alloy 800H can be given by

$$k = 10.784 + 2.588 \times 10^{-2} T - 3.051 \times 10^{-5} T^2 + 2.529 \times 10^{-8} T^3 \tag{74}$$

k is thermal conductivity in W/m-°C, and T is temperature in °C. Figure 25 plots both the tabulated data and function curve.

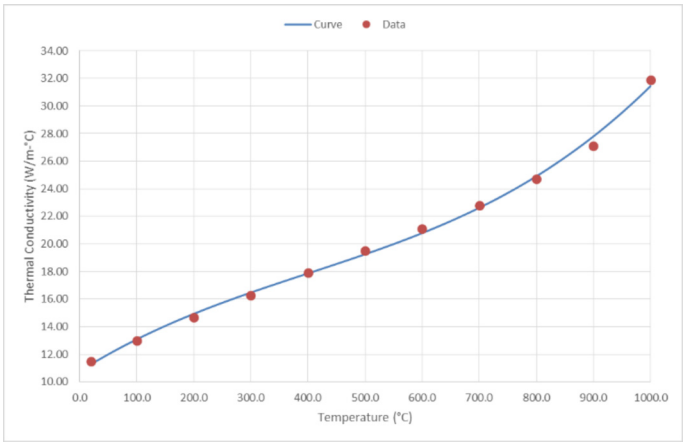

Figure 25. Thermal conductivity of Alloy 800H versus temperature.

9.2.1.3 MinWool-1200

The thermal conductivity of MinWool-1200 can be given by:

$$k = 2.927\times10^{-2} + 9.689\times10^{-5}T + 2.302\times10^{-7}T^2 - 5.742\times10^{-11}T^3 \quad (75)$$

k is thermal conductivity in W/m-°C, and T is temperature in °C. Figure 26 plots both the tabulated data and function curve.

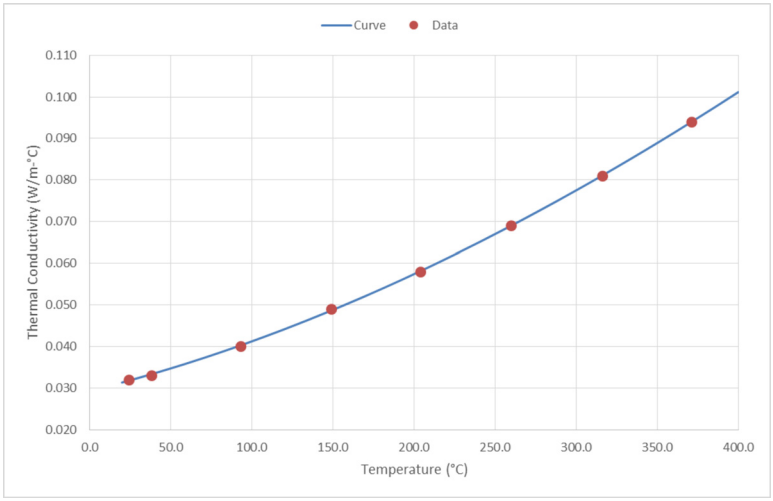

Figure 26. Thermal conductivity of MinWool-1200 versus temperature.

9.2.1.4 Thermo-12 Gold

The thermal conductivity of Thermo-12 Gold can be given by:

$$k = 5.023\times10^{-2} + 6.491\times10^{-5}T + 2.098\times10^{-7}T^2 - 1.420\times10^{-10}T^3 \quad (76)$$

k is thermal conductivity in W/m-°C, and T is temperature in °C. Figure 27 plots both the tabulated data and function curve.

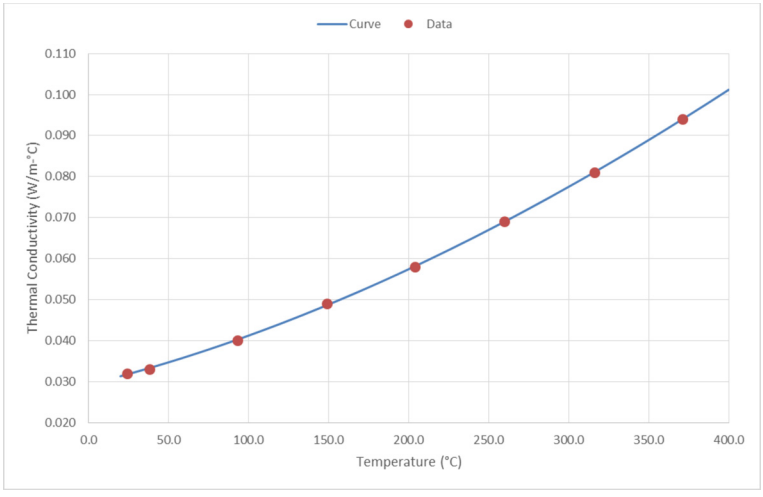

Figure 27. Thermal conductivity of thermo-12 gold versus temperature.

9.2.1.5 Sproule WR-1200

The thermal conductivity of Sproule WR-1200 can be given by:

$$k = 6.472\times10^{-2} + 7.501\times10^{-5}T + 2.898\times10^{-7}T^2 - 3.453\times10^{-10}T^3 \quad (77)$$

k is thermal conductivity in W/m-°C, and T is temperature in °C. Figure 28 plots both the tabulated data and function curve.

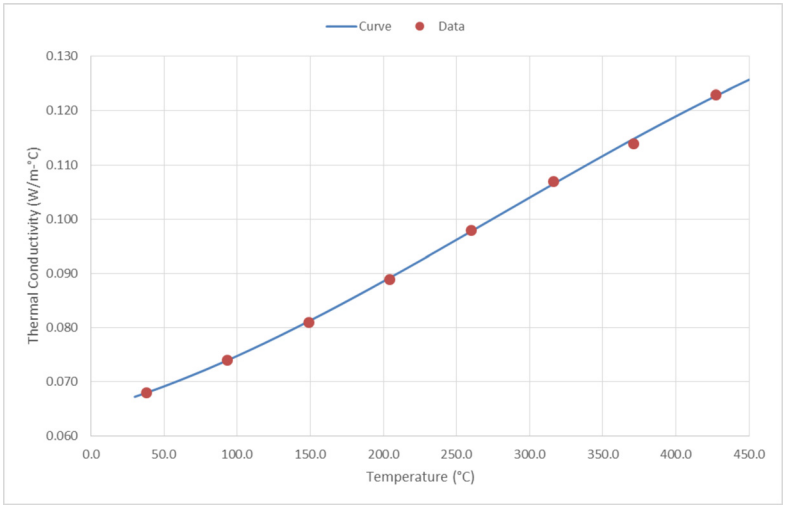

Figure 28. Thermal conductivity of Sproule WR-1200 versus temperature.

9.2.1.6 Pyrogel-XT

The thermal conductivity of Pyrogel-XT can be given by:

$$k = 1.990\times10^{-2} + 3.448\times10^{-5}T - 3.214\times10^{-8}T^2 + 2.778\times10^{-10}T^3 \quad (78)$$

k is thermal conductivity in W/m-°C, and T is temperature in °C. Figure 29 plots both the tabulated data and function curve.

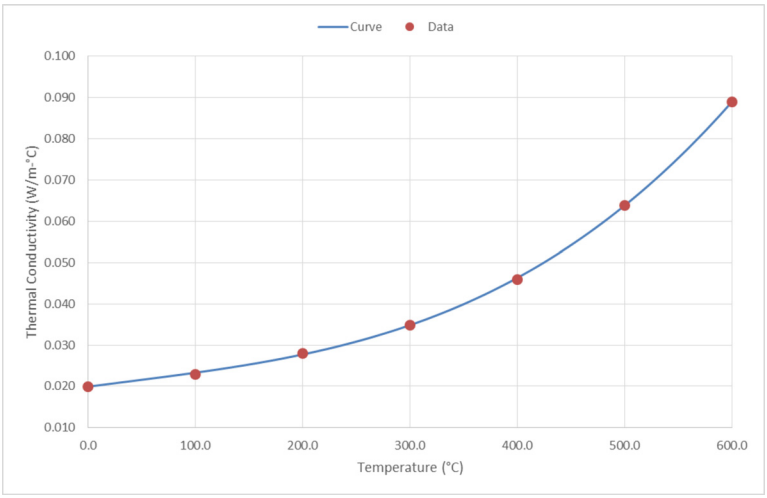

Figure 29. Thermal conductivity of pyrogel-XT versus temperature.

9.2.1.7 Microtherm Moulded Product

The thermal conductivity of Microtherm Moulded Product can be given by:

$$k = 2.600\times10^{-2} - 4.000\times10^{-5}T + 1.125\times10^{-7}T^2 - 6.250\times10^{-11}T^3 \quad (79)$$

k is thermal conductivity in W/m-°C, and T is temperature in °C. Figure 30 plots both the tabulated data and function curve.

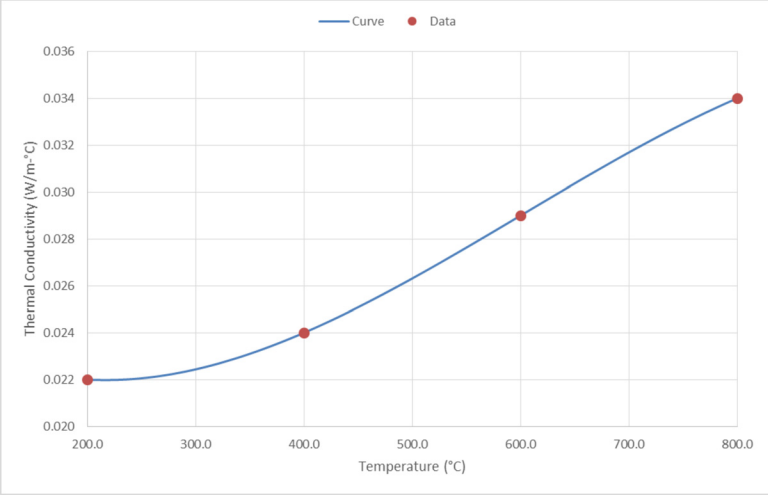

Figure 30. Thermal conductivity of Microtherm Moulded product versus temperature.

9.2.1.8 Molten Salt KF-ZrF_4

The property functions versus temperature of molten fluoride salt KF-ZrF_4 have been summarized in the literature (Lv. 2013), as shown below:

$$\rho = 3416 - 0.887(T - 273.1) \tag{80}$$

$$c_p = 1.046 \tag{81}$$

$$\mu = 0.159\mathrm{e}^{\frac{3179}{T}} \tag{82}$$

$$k = 0.0005T - .0320 \tag{83}$$

T is the temperature in K, ρ is the density in kg/m^3, c_p is the specific heat in kJ/kg-K, μ is the dynamic viscosity in mPa-sec, and k is the thermal conductivity in W/m-K.

9.2.1.9 Helium at 7 MPa

The tabulated data versus temperature of helium properties at 7 MPa can be found from National Institute of Standards and Technology (NIST) website [45]. The data can be fitted using *CurveExpert*, and the functions obtained are shown below:

$$\rho = 19.306 - 4.497\times10^{-2}T + 5.242\times10^{-5}T^2 - 3.048\times10^{-8}T^3 + 7.063\times10^{-12}T^4 \tag{84}$$

$$c_p = 5.1884 \tag{85}$$

$$\mu = 5.848 + 5.321\times10^{-2}T - 1.957\times10^{-5}T^2 + 8.447\times10^{-9}T^3 - 1.708\times10^{-12}T^4 \tag{86}$$

$$k = 4.303\times10^{-2} + 4.436\times10^{-4}T - 1.972\times10^{-7}T^2 + 9.607\times10^{-11}T^3 - 2.143\times10^{-14}T^4 \tag{87}$$

T is the temperature in K, ρ is the density in kg/m^3, c_p is the specific heat in kJ/kg-K, μ is the dynamic viscosity in μPa-sec, and k is the thermal conductivity in W/m-K. Figure 31, Figure 32, and Figure 33 plot the density, dynamic viscosity and thermal conductivity function curve compared with tabulated data.

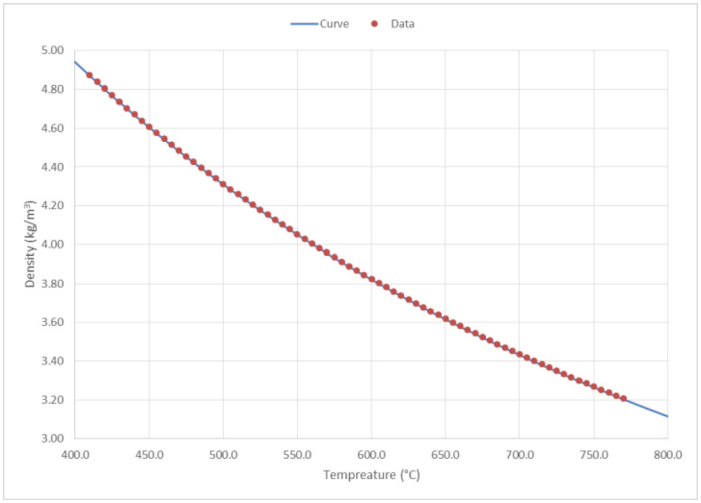

Figure 31. Density of helium at 7 MPa versus temperature.

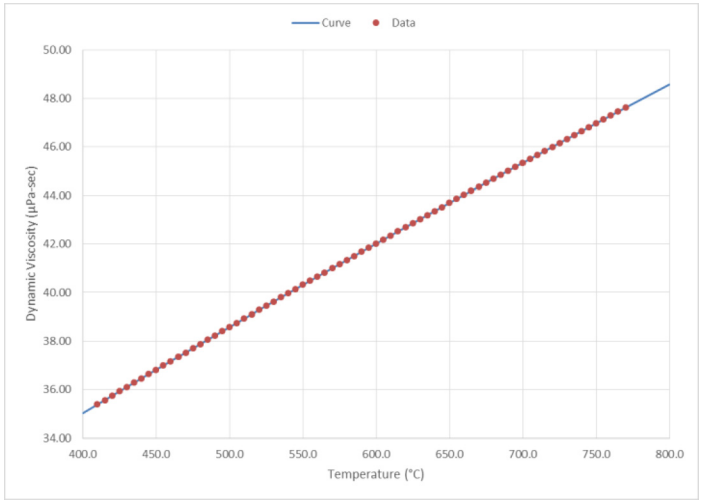

Figure 32. Dynamic viscosity of helium at 7 MPa versus temperature.

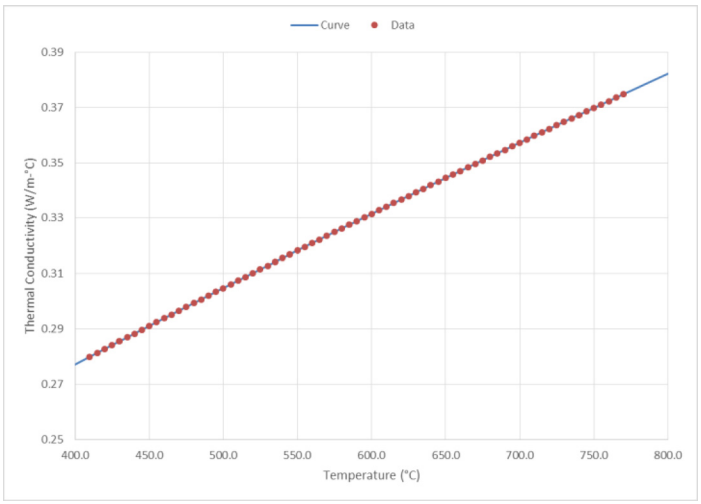

Figure 33. Thermal conductivity of helium at 7 MPa versus temperature.

10. REFERENCES

[1] Williams, D. F., and Clarno, K. T., "Evaluation of Salt Coolants for Reactor Applications," *Nuclear Technology*, Vol. 163, pp. 330–343, 2008.

[2] Sabharwall, P., Kim, E. S., McKellar, M., et al., *Process Heat Exchanger Options for the Advanced High Temperature Reactor*, Idaho National Laboratory, INL/EXT-11-21584, June 2011.

[3] Williams, D. F., Toth, L. M., Clarno, K. T., "Assessment of Candidate Molten Salt Coolants for the Advanced High-Temperature Reactor (AHTR)," Oak Ridge National Laboratory, ORNL/TM-2006/12, 2006.

[4] Lane, J. A., *Fluid Fuel Reactor*, Addison-Wesley Pub. Co., 1958.

[5] Sabharwall, P., Ebner, M., Sohal, M., et al., *Molten Salts for High Temperature Reactors: University of Wisconsin Molten Salt Corrosion and Flow Loop Experiments - Issues Identified and Path Forward*, Idaho National Laboratory, INL/EXT-10-18090, March 2010.

[6] Olson, L. C., *Materials Corrosion in Molten LiF-NaF-KF Eutectic Salt*, Ph.D. Dissertation, University of Wisconsin-Madison, Nuclear Engineering, 2009.

[7] Figley, J. T., *Numerical Modeling and Performance Analysis of Printed Circuit Heat Exchanger for Very High-Temperature Reactors*, MS Thesis, The Ohio State University, Nuclear Engineering, 2009.

[8] Rohsenow, W. M., Hartnett, J. P., and Cho, Y. I., *Handbook of Heat Transfer*, Third ed., McGraw-Hill, New York, New York, 1998.

[9] Mylavarapu, S. K., *Design, Fabrication, Performance Testing, and Modeling of Diffusion Bonded Compact Heat Exchangers in a High-Temperature Helium Test Facility*, Ph.D. Dissertation, The Ohio State University, Nuclear Engineering, 2011.

[10] Kim, I. H., No, H. C., and Lee, J. I., "Thermal Hydraulic Performance Analysis of the Printed Circuit Heat Exchanger Using a Helium Test Facility and CFD Simulations," *Nuclear Engineering and Design*, Vol. 239, pp. 2399–2408, 2009.

[11] Lv, Q., *Scaling Analysis for the Direct Reactor Auxiliary Cooling System for AHTRs*, MS Thesis, The Ohio State University, Nuclear Engineering, 2013.

[12] Ishii, M. and Kataoka, I., "Scaling Laws for Thermal-Hydraulic System under Single Phase and Two-Phase Natural Circulation," *Nuclear Engineering and Design*, Vol. 81, pp. 411–425, 1983.

[13] Todreas, N.E. and Kazimi, M.S., *Nuclear System I: Thermal Hydraulic Fundamentals*, 2nd ed., Taylor & Francis, Boca Raton, Florida, 2013.

[14] American Special Metals Homepage, Available at www.americanspecialmetals.com, accessed February 10, 2014.

[15] Haynes International, Inc. Homepage, Available at ww.haynesintl.com, accessed February 12, 2014.

[16] AK Steel Corporation Homepage, Available at www.aksteel.com, accessed February 13, 2014.

[17] Misra, A., J. Whittenberger, "Fluoride Salts and Container Materials for Thermal Energy Storage Applications in the Temperature Range 973 to 1400 K, National Aeronautics and Space Administration," NASA Lewis Technical Memorandum 89913, 1987.

[18] Anderson, M., et al., *University of Wisconsin-Madison Molten Salt Program- Experiments and Lessons Learned*, March 2010.

[19] Glosup, R. E., *Characterization of the High-Temperature Helium Facility in the Thermal Hydraulics Laboratory*, MS Thesis, The Ohio State University, Nuclear Engineering, 2011.

[20] Hart, G. H. and Yarbrough, D. W., "Industrial Insulation Systems: Material Selection Factors," *Chemical Engineering*, October 2010.

[21] ASTM Standard C547, 2012, "Standard Specification for Mineral Fiber Pipe Insulation", ASTM International, West Conshohocken, Pennsylvania, 2012, www.astm.org

[22] Industrial Insulation Group, LLC, homepage website, www.iig-llc.com, accessed on May 1, 2014.

[23] ASTM Standard C533, 2013, "Standard Specification for Calcium Silicate Block and Pipe Thermal Insulation," ASTM International, West Conshohocken, Pennsylvania, 2013, www.astm.org

[24] ASTM Standard C610, 2011, "Standard Specification for Molded Expanded Perlite Block and Pipe Thermal Insulation," ASTM International, West Conshohocken, Pennsylvania, 2013, www.astm.org.

[25] ASTM Standard C1728, 2013, "Standard Specification for Flexible Aerogel Insulation," ASTM International, West Conshohocken, Pennsylvania, 2013, www.astm.org.

[26] Aspen Aerogels, homepage website, www.aerogel.com, accessed on May 1, 2014.

[27] ASTM Standard C1676, 2008, "Standard Specification for Microporous Thermal Insulation," ASTM International, West Conshohocken, Pennsylvania, 2008, www.astm.org.

[28] Microtherm, homepage website, www.microthermgroup.com, accessed on May 1, 2014.

[29] ASTM Code C585, 2010, "Standard Practice for Inner and Outer Diameters of Thermal Insulation for Nominal Sizes of Pipe and Tubing," ASTM International, West Conshohocken, Pennsylvania, 2010, www.astm.org.

[30] Curve Expert Website, www.curveexpert.net, accessed on March, 2014.

[31] American Society of Mechanical Engineers and American National Standards Institute, 2007, *Process Piping ASME Code for Pressure Piping*, B31.3, New York, New York.

[32] Sinnott, R. K., *Chemical Engineering Design*, 4th ed., Elsevier Butterworth-Heinemann, Oxford, Massachusetts, 2005.

[33] Genic, S. B., Jacimovic, B. M., Genic, V. B., "Economic Optimization of Pipe Diameter for Complete Turbulence," *Energy and Buildings*, October 2011.

[34] Durand, A. A., Casas, M. J. V., et al., "Updating the Rules for Pipe Sizing," *Chemical Engineering*, January 2010.

[35] Shaffer, J. H., *Preparation and Handling of Salt Mixtures for the Molten Salt Reactor Experiment*, Oak Ridge National Laboratory, January 1971.

[36] Briggs, R. B., *Molten-Salt Reactor Program Semiannual Progress Report*, Oak Ridge National Laboratory, ORNL-3708, July 31, 1964.

[37] Scheele. R. D., and Casella. A. M., *Assessment of the Use of Nitrogen Trifluoride for Purifying Coolant and Heat Transfer Salts in the Fluoride Salt-Cooled High-Temperature Reactor*, Pacific Northwest National Laboratory, PNNL-19793, September 2010

[38] Kelleher. B. C., Sellers. S. R., et al., "Chemistry Control and Corrosion Mitigation of Heat Transfer Salts for Fluoride Salt Reactor (FHR)," *Proceedings of ICAPP '12, Chicago, USA, June 24–28, 2012.*

[39] Transactions in Measurement and Control, Volume 4, Flow & Level Measurement, www.OMEGA.com.

[40] Tallackson, J. R., Moore, R. L., Ditto, S. J., *Instrumentation and Controls Development for Molten-Salt Breeder Reactors*, Oak Ridge National Laboratory, ORNL-TM-1856, May 22, 1967.

[41] KROHNE Messtechnik GmbH, homepage website, www.krohne.com, accessed May 1, 2014.

[42] GE, homepage website, www.gesensing.com, accessed May 1, 2014.

[43] FLEXIM AMERICAS Corporation, homepage website, www.flexim.com, accessed May 1, 2014.

[44] Oceaneering International Company, homepage website, www.grayloc.com, accessed April 16, 2014.

[45] NIST Website, http://webbook.nist.gov/chemistry/fluid/, accessed on March 1, 2014.